Pore morphology in thermally-treated shales and its implication on CO_2 storage applications

A gas sorption, SEM, and small-angle scattering study

Chandra, Debanjan; Bakshi, Tuli; Bahadur, Jitendra; Hazra, Bodhisatwa; Vishal, Vikram; Kumar, Shubham; Sen, Debasis; Singh, T. N.

Important note
To cite this publication, please use the final published version (if applicable).
Please check the document version above.

Pore morphology in thermally-treated shales and its implication on CO_2 storage applications: A gas sorption, SEM, and small-angle scattering study

Debanjan Chandra [a,b], Tuli Bakshi [a], Jitendra Bahadur [c,d], Bodhisatwa Hazra [e], Vikram Vishal [a,f,g,*], Shubham Kumar [a], Debasis Sen [c,d], T.N. Singh [a]

[a] Computational and Experimental Geomechanics Laboratory, Department of Earth Sciences, Indian Institute of Technology Bombay, Mumbai 400076, India
[b] Department of Geoscience and Engineering, Delft University of Technology, 2628 CN Delft, the Netherlands
[c] Solid State Physics Division, Bhabha Atomic Research Centre, Mumbai 400085, India
[d] Homi Bhabha National Institute, Anushaktinagar, Mumbai 400094, India
[e] CSIR- Central Institute of Mining and Fuel Research, Barwa Road Campus, Dhanbad 826015, India
[f] National Centre of Excellence in Carbon Capture and Utilization, Indian Institute of Technology Bombay, Mumbai - 400076, India
[g] Interdisciplinary Programme in Climate Studies, Indian Institute of Technology Bombay, Mumbai - 400076, India

ABSTRACT

A combination of high-resolution imaging, low-pressure gas adsorption, and small-angle X-ray and neutron scattering quantifies changes in the pore characteristics of pulverized shale samples under oxic and anoxic environments up to 300 ℃. Clay-rich early-mature shales have a fair potential to generate hydrocarbons, the total organic carbon content of which lies within a range of 2.9 % to 7.4 %. High-resolution imaging indicates restructuring and coalescence of Type III kerogen-hosted pores due to oxic heating, which causes up to 580 % and 300 % increase in the surface area and pore volume of mesopores respectively. Similarly, up to 300 % and 1200 % increase in micropore surface area and pore volume is observed post oxic heating. However, during anoxic heating, bitumen mobilizes, leads to pore-blockage, and reduces the surface area and pore volume up to 45 % and 12 % respectively without any significant mass loss up to 350 ℃. Between 400 and 550 ℃, considerable loss in mass occurred due to breaking of organic matter, facilitated by the presence of siderite that caused up to 30 % loss in mass. The test conditions display starkly opposite effects in pores that have a width of < 100 nm when compared to the larger macropore domain, which has a pore width in the range of 100 to 700 nm as inferred from their small-angle X-ray (SAXS) and neutron (SANS) scattering behaviour, respectively. Despite the formation of new mesopores or the creation of new networks of pores with rougher surfaces, the fractal behavior of accessible mesopores in combusted shales minimally increase mesopore surface roughness. The pyrolyzed shales exhibit decreased mesopore surface roughness at higher temperatures, which indicates smoothening of pores due to pore blocking. Increase in pore volume and surface area due to oxic-heat treatment enhances the feasibility of long-term CO_2 storage in shales.

1. Introduction

Conventional fossil fuels have been intensively used as a source of energy since a long time. However, the gradual depletion and the environmental effects due to increasing amounts of greenhouse gases have prompted the development of cleaner, unconventional fuels. The plentiful reserves of shale gas and it being a low-carbon energy resource, have already attracted worldwide interest. However, the extraction of shale is challenging due to its heterogeneity, low permeability, and complicated pore system that comprises a wide variety of pore types and pore size distributions (PSD) [1–5]. These features directly influence gas storage and transport behavior in the shale matrix [6–9]. Jamaluddin et al. (2000) [10] have suggested that a rise in temperature significantly modifies the characteristics of shale pores. The effect of pyrolysis on kerogen has been investigated extensively [11–14]. Researchers have suggested combustion and pyrolysis treatment to recover shale gas [15,16], which facilitates the desorption of gas from pores, expedites permeability, and acts as an alternative to fracking [17–19]. It has been

---

* Corresponding author at: Computational and Experimental Geomechanics Laboratory, Department of Earth Sciences, Indian Institute of Technology (IIT) Bombay, Powai, Mumbai - 400076, India.
E-mail address: v.vishal@iitb.ac.in (V. Vishal).

established that combustion or pyrolysis regenerates and reopens the already existing kerogen micro- and mesopores by structurally altering them [20,21]. As a result, effective porosity increases, which leads to an improved flow of gas in the matrix. Nanopores and microfractures have recently received attention in shale gas recovery research due to their significant effects on permeability [22,23]. The altering of wettability and flow behaviors in shales due to kerogen maturity and the presence of bitumen has been studied in detail [24–27]. However, the evolution of the pore system during thermal treatment involves complex physico-chemical processes. Thermal treatment of shales in presence of oxygen have shown widely varying changes in organic matter porosity, composition and mechanical properties. A recent study by Zhang et al. (2021) using small-angle X-ray scattering (SAXS) has shown that the peak thermal decomposition for organic matter in shale is at 500 ºC and that of inorganic matter is 750 ºC [28]. Zhu et al. (2021) simulated the effect of microwave heating in shales using a fully coupled thermo-hydraulic-mechanical-chemical (THMC) model and concluded that the thermal stress in shales increases sharply during early stage of progressive heating and then reduces gradually [29]. Heating beyond 100 ºC also induces microcracks in shales, thereby causing loss of strength properties [30]. Extreme heating of shales up to 900 ºC shows morphological changes in organic matter along with dihydroxylation of clay minerals and decomposition of calcite [31]. X-ray CT imaging coupled with in-situ thermal treatment highlights selective formation of void spaces in organic rich part of shale cores implying enhancement of pore spaces [32] and such pore spaces are pervasive and contributes to a thousandfold increase in mass transfer coefficient [20,33,34]. Cyclic thermal treatment of shales promotes generation and logarithmic expansion of pores depending on the number of heating cycles [35]. Heating also enhances the gas desorption behavior from shale matrix, contributing in enhanced gas recovery from shale reservoirs [36]. All of these studies have been performed under oxic environment and very limited information is available to compare the contrasting response of shales under oxic and anoxic environment, as the chemical changes of organic matter will drastically vary between these two conditions. Moreover, observation in these studies are limited to micro and meso-pore range, whereas the dynamics of macropores remain unclear..

With vast global abundance and high porosity, shale reservoirs have proven to be a possible sink for large volume of CO_2 storage [37–39]. However, the extremely low permeability in shales have proven to be a major disadvantage in terms of CO_2 storage operations. Recent studies have proven that CO_2 storage in fractured and depleted shale reservoirs are cheaper than storage in saline aquifers, and the cost of operation is further reduced in an integrated carbon capture and storage (CCS) system [40]. A comprehensive numerical study of long-term CO_2 storage potential in North American shale formations have shown an efficiency factor of 0.15 to 0.36 for CO_2 storage as free phase and an efficiency factor of 0.11 to 0.24 for CO_2 storage as adsorbed phase [41]. A case study on Marcellus shales have shown an incremental gas production of 7 % and a total recovery efficiency of 32 % during CO_2 mediated enhanced shale gas recovery [42]. Xu et al. (2017) [43] used a triple porosity, dual permeability model to understand dynamics of enhanced shale gas recovery with CO_2 injection and concluded that the recovery factor is directly proportional to the organic content. However, the CO_2 storage capacity gradually decreases due to matrix swelling and permeability reduction. Experimental studies have also indicated opening of micro-scale pores and closure of nano-scale pores in shales due to CO_2 exposure, leading to significant alteration of fracture and matrix permeability [39,44–46]. A reservoir scale simulation of CO_2 injection in New Albany Shales indicated a very low breakthrough of CO_2 and a 95 % efficiency of CO_2 trapping through adsorption processes [47], indicating CO_2 injection in shale to be a viable and safe pathway for CO_2 mitigation. The same was iterated in a field scale CO_2 storage operation in Morgan County, Tennessee [48]. Although CO_2 injection have been identified as feasible pathways for enhanced shale gas re-covery, the alteration in porosity, specifically the reduction in porosity

due to shale-CO_2 interaction proves to be a bottleneck for commercial long-term operation. A fully coupled thermo-hydro-mechanical (THM) model proposed by Liu et al. (2020) [49] explains how thermal treat-ment of shale reservoirs eliminates the water lock effect, facilitates gas desorption, and enhances permeability by creating microcracks. This in essence creates more pore spaces for CO_2 storage, however, such pore-scale insights lack in previous studies. A reservoir simulation study on sequential combination of in-situ pyrolysis and combustion treatment proves that such protocol also reduces the energy requirement, and fa-cilitates gas recovery, albeit with higher CO_2 production from the reservoir due to the thermal treatment [50]. With such limited avail-ability of pore scale experimental studies on the combination of thermal treatment and CO_2 storage, this study takes a unique approach to explore the benefits of thermal stimulation in shale which might coun-terbalance the operational setbacks of CO_2 injection in shale reservoirs.

In this study, we attempt to explore the physicochemical changes that occur in kerogen pores with increasing temperature, in the presence and absence of oxygen by using a combination of gas adsorption and scattering measurements. The changes in pore attributes and pore accessibility and its driving factors due to thermal treatment under both conditions are explored in this study. Impact of mineral and kerogen composition on the extent of thermal changes are also highlighted along with their role in enhancing the storage capacity of CO_2 in shale reser-voirs. Findings of this study will help understand the applicability and effectiveness of thermally enhanced shale gas recovery. Changes in pore attributes and their connectivity will also help assess the feasibility of CO_2 storage in shale reservoirs.

2. Experimental procedure

2.1. Geological setting

Shale samples were collected from an active logging site at Gour-andih in Asansol, belonging to the Raniganj Basin and is of Late Permian age Barakar Formation (Fig. 1). Raniganj Basin contains very thick organic rich shales having a high prospect of shale gas exploration [51,52]. The basin is located between 23°22′N and 23°52′N latitudes and 86°36′E and 87°30′E longitudes [53]. Two dominant sets of fault trending NNE-SSW and NNW-SSE and the mafic intrusion known as Salma dike gives Raniganj Basin a complex geological setting [54]. In terms of lithostratigraphy, the basement is composed of Precambrian metamorphic rocks, overlain by Permian age glaciogenic sediments of Talchir Formation, followed by younger Raniganj, Barren Measures and Barakar Formations respectively. The shales from this study were collected from Barakar Formation, which comprises conglomerates, gritty to pebbly crossbedded sandstones and siltstones with interlayer-ing of black shales and coal [55]. Signatures of tidal and wave reworking were found in upper parts of Barakar Formation with distinct basal fluvial and upper tidal wave mediated fluvio-marine depositional system [56].

Four shale samples were collected as cores from a depth range of 354–671 m (Table 1). The samples SH3, SH6, SH9 and SH15 were packed in airtight bags immediately after logging in order to minimize any alteration. The shale cores were powdered and screened using the ASTM 210 and 230 mesh size in series. The remaining grains of size ~ 250 μm on the 230-mesh sieve were collected for Rock-eval pyrolysis, small-angle X-ray (SAXS) and neutron (SANS) scattering, thermo-gravimetric analysis (TGA), and low-pressure gas adsorption study (LPGA). The powders were divided into two sets to be subjected to the oxic and anoxic heating environment. Each sample were further split into different batches and heated at 100 °C, 200 °C, and 300 °C, respectively. The oxic heating were performed in a hot air oven whereas the anoxic heating was performed in a vacuum oven with a pressure in the range of 10^{-4} bar. The heating rate for both oxic and anoxic heating were selected as 10 °C/min, followed by a 24 h hold time. The anoxic-heated samples were allowed to cool inside the vacuum oven to
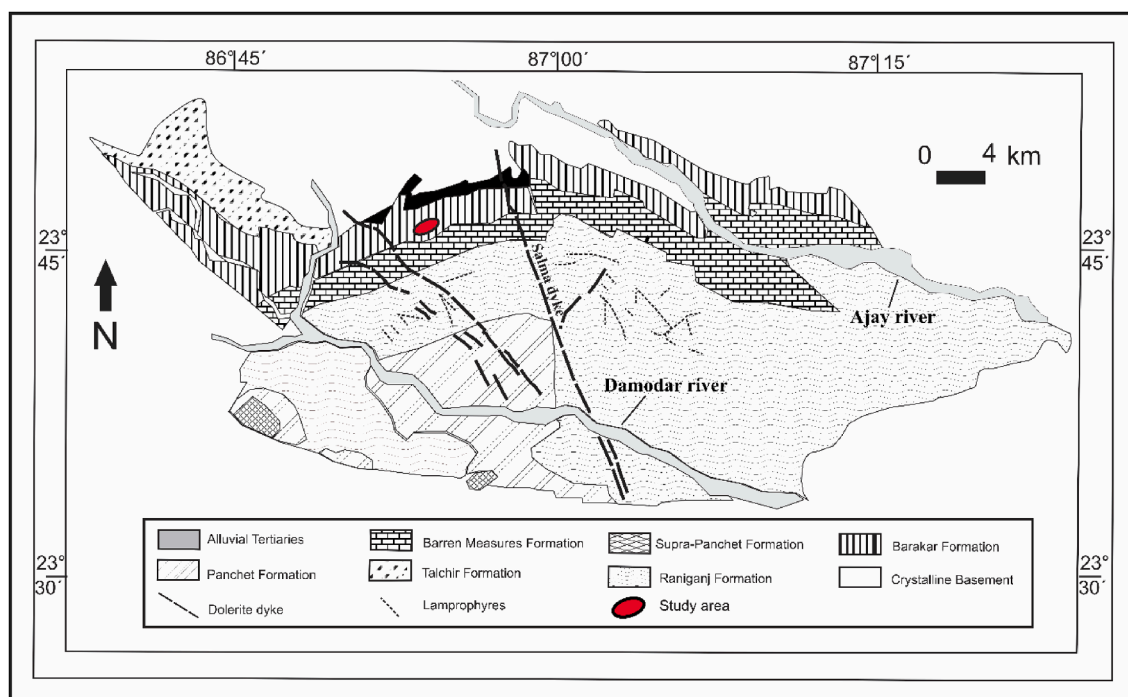
Fig. 1. Raniganj Basin with the sample location (after Gee, 1932).

Table 1
Mineral composition and organic matter properties of the shales. All mineral compositions are represented as wt%.

Sample	Depth (m)	S1 (mg/g)	S2 (mg/g)	S3′ (mg/g)	Tmax (°C)	PC (%)	RC (%)	TOC (%)	HI
SH3	354	0.3	2.96	58.8	444	0.41	5.13	5.54	53
SH6	422	0.69	9.87	55.6	441	1.09	6.27	7.36	134
SH9	593	0.18	1.92	38.5	446	0.26	2.53	2.79	69
SH15	671	0.3	2.73	193.2	454	1.09	2.59	3.68	74
				Mineral compositions					
Sample	Quartz	Kaolinite	Illite	Siderite	Calcite	Muscovite	Biotite	Pyrite	Ilmenite
SH3	26.1	35.7	4.1	9.5	4.6	12.8	5.9	1.3	–
SH6	13.6	36.5	4.2	10.4	1.8	30.2	3.3	–	–
SH9	38.4	37.6	3.9	3.1	1.3	8.9	6.8	–	–
SH15	5.2	–	–	39	48.4	–	–	5.2	2.2

*S1 = The free hydrocarbons present in the sample before the analysis, S2 = The volume of hydrocarbons that formed during thermal pyrolysis of the sample, S3′ = inorganic CO_2 produced during the pyrolysis stage, PC = pyrolyzable carbon, RC = residual carbon, TOC = total organic carbon, HI = hydrogen index.

minimize any interaction with atmospheric oxygenated air with the heated samples. To maintain consistency in the cooling protocol, oxic-heated shales were also allowed to cool inside the oven. Additionally, the images acquired from the field emission gun-scanning electron microscopy (FEG-SEM) visualize the changes in the shale pores caused by the thermal treatment.

2.2. Small-angle scattering

Small-angle scattering (SAS) is a non-destructive method to characterize micro and nanoporous media such as shale and coal [57,58]. This technique is implemented to determine the density fluctuations in materials in 1–500 nm range. The pores in shale are regarded as inhomogeneities that give rise to scattering of X-rays/neutron at small angle regime. Thus, SAS is a bulk-sensitive technique, that provides statistically averaged information about pore size and shapes. A combination of small-angle neutron scattering (SANS) and small-angle X-ray scattering (SAXS) techniques was leveraged to characterize the hierarchical structure of shale pore by accessing a wide range of wave vector transfer (Q). Unlike gas adsorption or imaging techniques, SAXS and SANS techniques are better suited for characterizing accessible and inaccessible pores, providing a more realistic pore characteristic of

shales. Raw data from SAS analysis were recorded as the change in intensity I(Q) with the change in Q. For this study, powdered shales heated as per protocol (Fig. 2) were packed between two Kapton tapes and mounted on the sample holder of the SAXS facility with a micro-focus CuK_α (λ = 1.54 Å) source. 2D SAXS data recorded in transmission mode were radially averaged to obtain a 1D scattering profile. SAXS intensity (I(Q)) was recorded as a function of Q, defined as $Q = 4\pi sin\theta/\lambda$, where 2θ is the scattering angle, and λ is the wavelength of the probing radiation. The wavelength of the neutrons for the SANS experiments was 3.12 Å. The Q range for the SAXS experiment was between 0.01 Å^{-1} to 0.13 Å^{-1}. The sample to detector distance for SAXS measurements was ~ 1 m and the X-ray beam size was 500 μm. To access the scattering intensity at further low-Q regime, the double-crystal based medium resolution SANS facility at the Dhruva reactor, Bhabha Atomic Research Centre (BARC) [59,60]. The accessible Q range for the SANS experiments was between 0.0005 and 0.017 Å^{-1}. The SANS data were further corrected for the instrument resolution. After background correction and noise removal, the pore attributes from the scattering data were calculated using the MATLAB-based code MATSAS [61]. The pore size distribution (PSD) has been calculated based on the poly-disperse spherical (PDSP) model (Fig S2, S3) (detailed description in Supplementary Material), which is suitable for randomly oriented
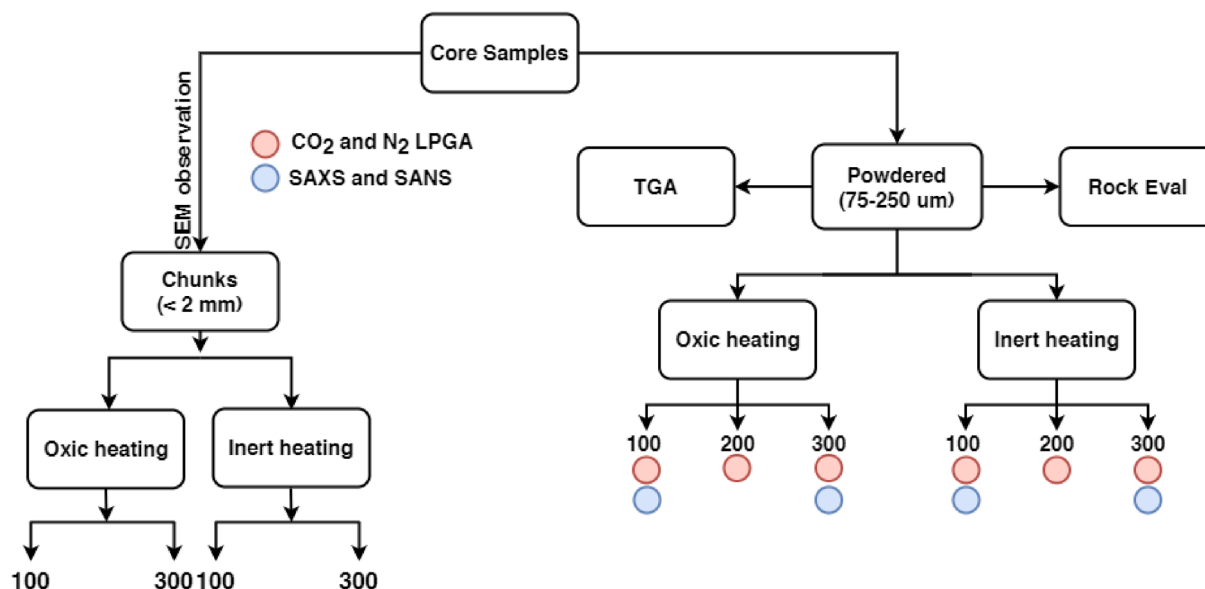
Fig. 2. Experimental procedure followed in this study. The scattering studies were performed for shales heated at 100 °C and 300 °C only.

independently scattering particles such as shale [57,58].

2.3. Field emission scanning electron microscopy

FEG-SEM imaging visualizes the pore structure characteristics and when combined with statistical methods, a quantitative characterization of the pore attributes is obtained. Furthermore, the FEG-SEM images distinguishes pores of different shapes and sizes in organic matter, minerals, and their respective grain boundary. For this study, a JEOL JSM-7600F FEG-SEM apparatus was used with a working distance of 5.7–6 mm and an operating voltage of 15 keV. The shale chunks were dried and Pt sputter-coated before imaging to enhance the scanning surface conductivity. SEM images can identify minerals and organic matter. Substrate which is good conductor of electrons appear as bright pixels, whereas bad conductors appear as darker. Pores are essentially void spaces, thereby having poor conductivity and are thus represented by dark pixels. On the other hand, minerals in shales (mainly alumino-silicates) are better conductor of electrons compared to organic matter (composed of organic carbon), owing to their brighter appearance.

2.4. Compositional characterization

The bulk mineral composition of the shale was assessed through XRD analysis. 2–3 mg of powdered shale was used to determine the diffractogram in PANalytical's X' Pert Pro instrument at the Department of Earth Sciences, IIT Bombay. The setup is equipped with a Cu anode and has a 40 kV of maximum operating voltage. The peaks were taken within a 2θ range of $5°$ and $70°$ with a scan step of $0.0130°/s$. The semi-quantitative mineralogy was analyzed using Rietveld refinement in the PANanalytical's HighScore Plus software. For characterization in terms of source rock properties, the samples were crushed to 212 μm size and analyzed using a Rock-Eval 6 device. 5–10 mg powdered shales were used for the built-in 'Basic/Bulk-Rock method' employed for the experiments, with the final temperature of the oxidation stage maintained at 750 °C. In this cycle, the samples loaded in crucibles were automatically inserted into the pyrolysis oven at first and heated isothermally at 300 °C, during which the free hydrocarbons or thermovapourizable components were released and registered under the S1 curve. This was followed by the samples being heated from 300 °C to 650 °C using the pre-defined 25 °C/min heating rate wherein the kerogen within the samples crack and generate heavier hydrocarbons, as registered under the S2 curve. The T_{max} (thermal maturity proxy) is calculated from the

S2 peak. Oxygenated compounds present within the organic matter and certain carbonate minerals such as siderite also crack during the pyrolysis stage, generating CO_2, detected by the IR detector and presented as S3 and S3′, respectively. The pyrolyzable carbon (PC) content is calculated from the pyrolysis stage. Following the pyrolysis stage, the samples were automatically transferred to the oxidation oven, where they were combusted in the presence of oxygen, yielding the residual carbon (RC) content. The Total Organic Carbon (TOC) content is calculated by adding PC and RC.

2.5. Thermogravimetric analysis

A thermogravimetric analyzer (Netzsch STA449 F1 Jupiter) was used to investigate the mass loss behavior of the shales under an anoxic heating environment. The analysis was performed in a nitrogen atmosphere having a 50 ml/min flow rate in the temperature range of 30–600 °C. The temperature range was selected to observe the behavior of the shales post our heating limit. The heating rate was set at 5 °C/min to maintain consistency of the heating program used for pre-treatment of the powders before other studies, and approximately 60 mg powdered samples were used for the experiment. The mass loss behavior with respect to time was further analyzed using differential thermal analysis (DTA) with the help of bundled software (Netzsch Proteus).

### 2.6. Low-pressure $N_2 – CO_2$ gas adsorption

Low-pressure gas adsorption has emerged as a useful technique for micro and mesopore characterization in shale [62–67]. Before the low-pressure adsorption analysis, thermally treated shales were degassed for 12 h in the presence of oxygen at room temperature under a vacuum to remove volatiles and moisture from sample pores. The heating program for the anoxic-heated samples, which were heated up to 300 °C, was performed in the degassing chamber of the instrument under vacuum. According to IUPAC nomenclature, pores are classified based on their sizes as micropores (<2 nm), mesopores (2–50 nm) and macropores (>50 nm) [68]. A Quantachrome Autosorb iQ single station physisorption analyzer was used for the analysis. N_2 was used to characterize *meso-* and macropores of shales. CO_2 at 0 °C can access micropores with < 2 nm diameter. Hence, a combination of N_2 and CO_2 isotherms characterizes micro- to larger mesopore range. For N_2-LPGA, adsorbed gas volume was measured in the relative pressure (P/P_0) range of 0.01–0.99, where P is the vapor pressure and P_0 is the saturation

pressure of nitrogen (760 torrs) at liquid nitrogen temperature (-196 °C). For CO_2-LPGA, the relative pressure range was selected as 0.005 to 0.03, where the saturation pressure of CO_2 at 0 °C is 26610 torr. The mesopore surface area was determined using the multipoint Brunauer–Emmett––Teller (BET) equation, while the Dubinin-Radushkevich (DR) method was used for micropore surface area determination. Mesopore size distribution (PSD) was calculated from the adsorption branch of N_2 isotherm using the Barrett-Joyner-Halenda (BJH) model and slit and cylindrical pore geometry-based quenched surface density functional theory (QSDFT) method. The PSD for micropores was calculated from the adsorption branch of the CO_2 isotherm using CO_2 upon the carbon DFT model. DFT with appropriate parameters links molecular simulations to classical thermodynamics [69]. Compared to classical NLDFT (non-local DFT), the QSDFT model incorporates the surface heterogeneity of the carbon and provides an improved adsorption isotherm [70,71].

3. Results

3.1. Shale composition and thermal maturity

The mineral composition of the shales (Table 1), show the dominance of clay minerals, quartz, siderite, and biotite. The TOC content varies between 2.79 and 7.36 wt%. Detailed mineral composition of the shales has been discussed in Chandra et al. (2021) [72]. SH15 is rich in siderite and indicates a late mature stage (Table 1) representing the peak oil generation stage. SH15 also reveals exceptionally high S3′ (193.2 mg CO_2/g rock). Rock-eval Tmax is a well-established thermal maturity, which is extremely reliable subject to the shape of the S2 curve and FID signal. For the studied suite of samples, the FID signal was observed to be within reliable limits (i.e. > 0.1 mV and < 125 mV) [73–75]. The S2 pyrograms of the studied shales (Fig S1) are reliable, and consequently, it can be inferred that the Tmax calculation is precise. Additionally, we would also like to point, out that generally, coals from the Raniganj
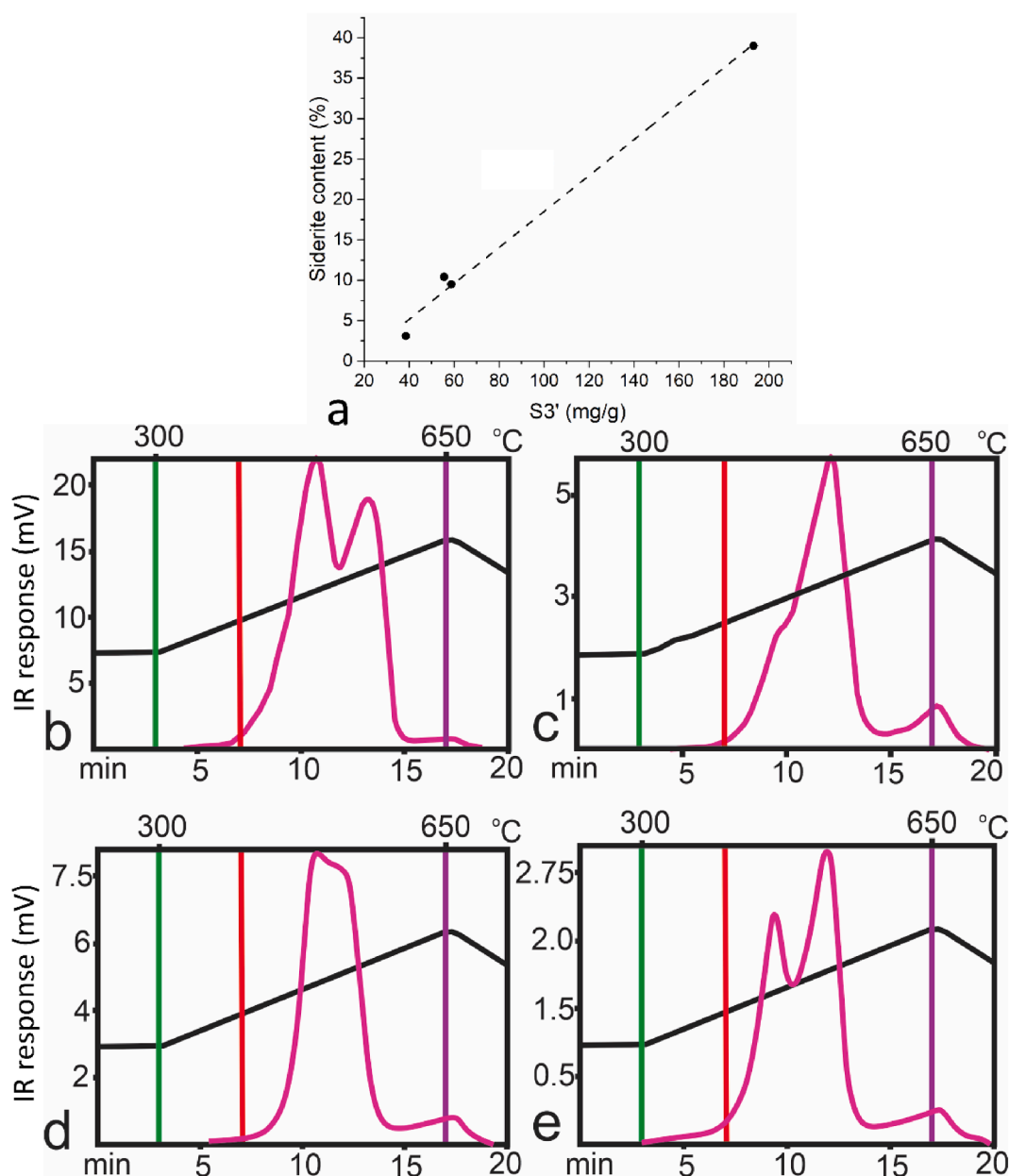
Fig. 3. (a) Positive correlation is observed between siderite concentration (determined using XRD) and S3′ of Rock-Eval (inorganic CO_2 produced during the pyrolysis stage), (b) S3′ pyrogram of (b) SH15, (c) SH9, (d) SH6 and (e) SH3.

basin present a high volatile bituminous rank (HvbA) [76]. For the studied suite, the Tmax varies between 441 ℃ and 454 ℃, i.e. estimated vitrinite reflectance of 0.78 % and 1.01 % (i.e. precisely in oil-window, similar to high volatile bituminous A rank for coals). For such cases, estimated VRo%= 0.0180 × Tmax – 7.16 [77,78].

Ideally, CO and CO_2 from organic matter are released below 400 ℃ and are represented by S3. Carbonate minerals such as siderite also decompose during Rock-Eval pyrolysis stage generating CO, CO_2 at temperatures > 400 ℃ and are represented as S3′. Thus, elevated S3′ signals indicate presence of siderite [79,80]. We referred to Hazra et al. (2022) [80] (and references within it) for understanding the impact of siderite on Rock-Eval S3 and S3′. For the studied suite of samples, S3′ was observed to be similar for samples SH3 and SH6 (58.8 and 55.6 mg CO_2/g rock, respectively) (Table 1). XRD analysis revealed presence of similar siderite content within these two samples (10 wt%). In contrast, S3′ was observed to be minimum for sample SH9 (38.5 mg CO_2/g rock), while SH15 showed the highest S3′ (193.2 mg CO_2/g rock). These two samples also showed the least (3 wt%) and highest (39 wt%) siderite contents, respectively. Consequently, a strong positive correlation was observed between siderite content and Rock-Eval (Fig. 3a).

Fig. 3b and c represent the S3′ pyrograms of SH15 (highest concentration of siderite) and SH9 (least siderite concentration) respectively.

The significant difference in the S3′ for both these samples indicate the difference in CO_2 produced from mineral carbonates (Table 1). SH15 having higher siderite conc. shows higher IR response (Fig. 3b) and vice versa for SH9 (Fig. 3c). The green line indicates the end of the isothermal stage (300 ℃). The red line in Fig. 3b and c represents the S3-S3′ boundary at 400 ℃, i.e., the demarcation between CO_2 from organic matter and CO_2 from mineral matter generated during pyrolysis. The purple line represents the end temperature of the pyrolysis stage (650 ℃). The PC/RC ratio is used as a proxy for the reactivity of the organic matter. PC/RC is highest for the SH15 shale (Table 1), indicating that the sample SH15 is more reactive during pyrolysis.

3.2. SEM imaging

Disposition of pores (Figs. 4 and 5), represent two separate cases when heated to 300 ℃, under oxic and anoxic, respectively. Intergranular pores (Fig. 4b, f, and 5e) are formed by vacant spaces in between quartz, feldspar, and clay minerals. Organic pores (Fig. 4a, c-e; 5a-d), as well as pores at the interface of organic matter and minerals form unique geometry (Fig. 4c). The OM pores show circular/semi-circular cross-section and occur in clusters [81–83]. 3D layered sheet-like structures are visible in clay minerals (Fig. 4b and f, 5e, and f). Microfractures are
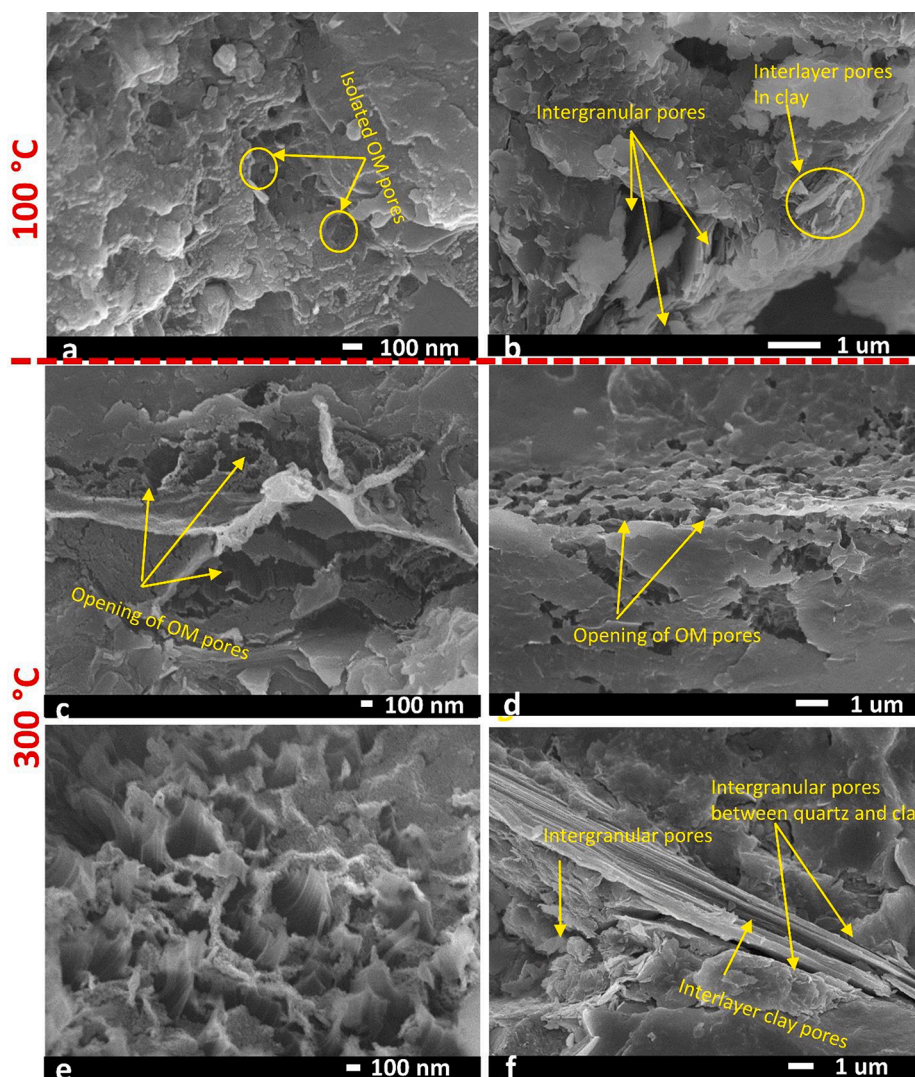
Fig. 4. Matrix in shale showing different types of pores (a); Isolated organic matter (OM) pores (b); Intergranular pores between clay mineral and quartz/feldspar grain, interlayer clay pores (c), (d), and (e); Opening of isolated OM pores and pore networks in shale combusted at 300 ℃ (f); intergranular and intragranular mineral pores at 300 ℃.
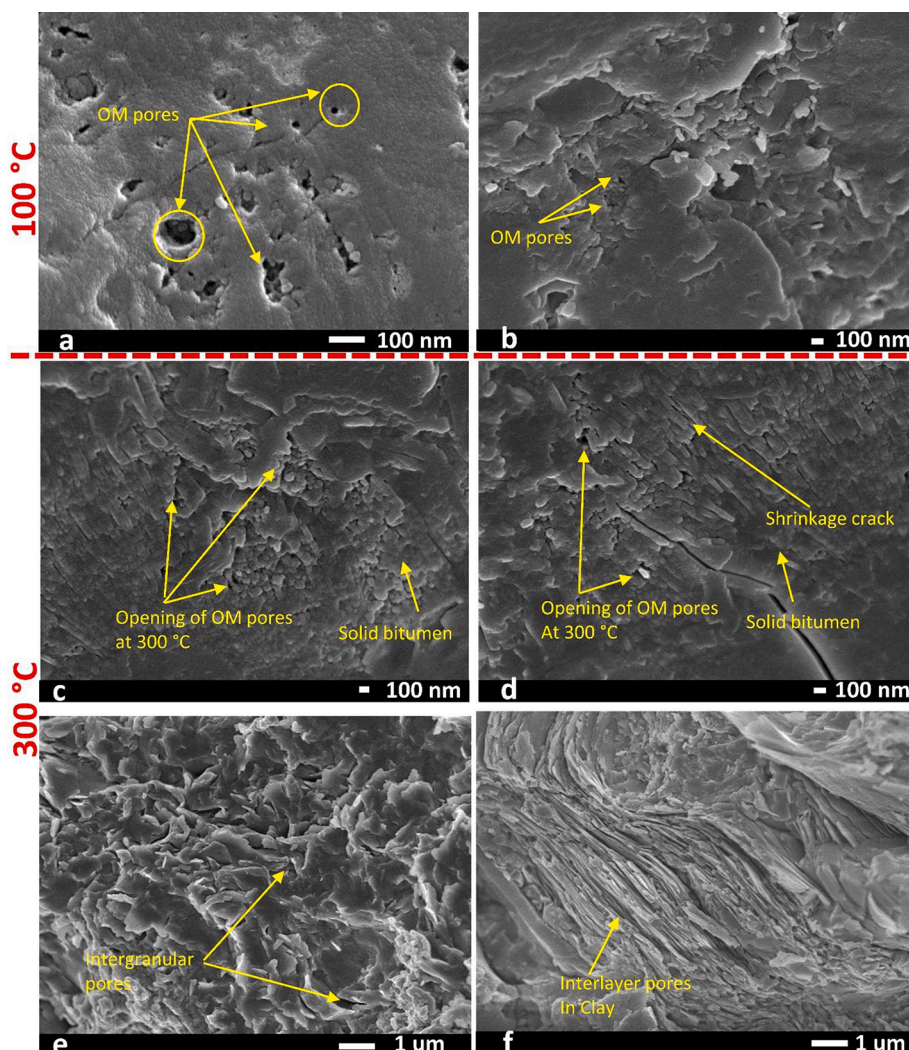
Fig. 5. Shale SEM images showing changes in pore structure, when heated to 300 ℃ in the absence of oxygen (a) & (b); Isolated organic matter (OM) pores at untreated samples (c) & (d); Spongy connected pores in organic matter at 300 °C, pores at higher temperature and shrinkage cracks (e) & (f); intergranular pores among OM, clay and other minerals, interlayer pores in clay at 300 °C.

visible in the organic matter (Fig. 5d).

Isolated circular OM pores can be seen in 100 ℃ heated samples (Fig. 4a, 5a,b). However, when heated at 300 °C in oxic and anoxic conditions, the pore characteristics change significantly. Isolated smaller mesopores in kerogen expand into macropores, enhancing pore connectivity (Fig. 4c,e and Fig. 5c,d). Spongy pores in organic matter (Fig. 4e) develop a well-connected pore network with rising temperature. However, Fig. 5c and d showcase a lack of larger pore network.

### 3.3. Scattering behavior of the shales

The scattering profiles of the anoxic-heated (Fig. 6a) and oxic-heated (Fig. 6c) shales show a linear trend in logarithmic plots indicating fractal nature. For such fractal system, the scattering intensity manifests a power law behaviour and thus the scattering intensity shows linearity in double logarithmic scale with respect to Q.

In all samples except SH15 pore volume decreases with increasing temperature when heated in an anoxic environment (Fig. 6b). The PSD plots at 100 °C and 300 °C show similar peak positions, although a major pore volume reduction is noticed in the smaller mesopore range. At 300 °C, SH15 shows sharp peaks at a smaller mesopore range, which is contrasting to that for other shale samples.

A noticeable increase in pore volume is observed at 300 °C for all the

shales when heated in presence of oxygen (Fig. 6d). The changes in PSD are further emphasized in the smaller mesopore range (3–10 nm pore width) for all the shales. While the peak positions of PSD curves are consistent in both temperatures, SH6 shows sharp increase in pore volume at a higher temperature within 3–8 nm pore width range.

SAXS and SANS data (Fig. 7) covers high (0.01–0.13 Å^{-1}) and low Q (0.0005–0.017 Å^{-1}), respectively and thereby provide information about the pore attributes of mesopore and macropore region. For the anoxic-heated shales, SH15 shows a slight deviation from the ideal fractal behaviour at a lower Q-range (Fig. 7a). In the SAXS derived PSD, at the mesopore and micropore range, the pore volume decreases with increasing temperature. Although the mesopore volume of anoxic-heated shales are lesser, macropore volume increases considerably in 100–400 nm pore size range for SH3, SH9 and SH15 (Fig. 7b). The extent of pore volume increase becomes insignificant post 400 nm pore width. For the oxic-heated shales distinct behaviour in shale pore volume alteration with heating. For SH3, mesopore volume increases with temperature, however with increasing pore width, lesser pore volume increase is observed (Fig. 6d). In the macropore range, the trend reverses in SANS-derived PSD (Fig. 7d). For SH15, both the SAXS and SANS derived PSD increase with increasing temperature.
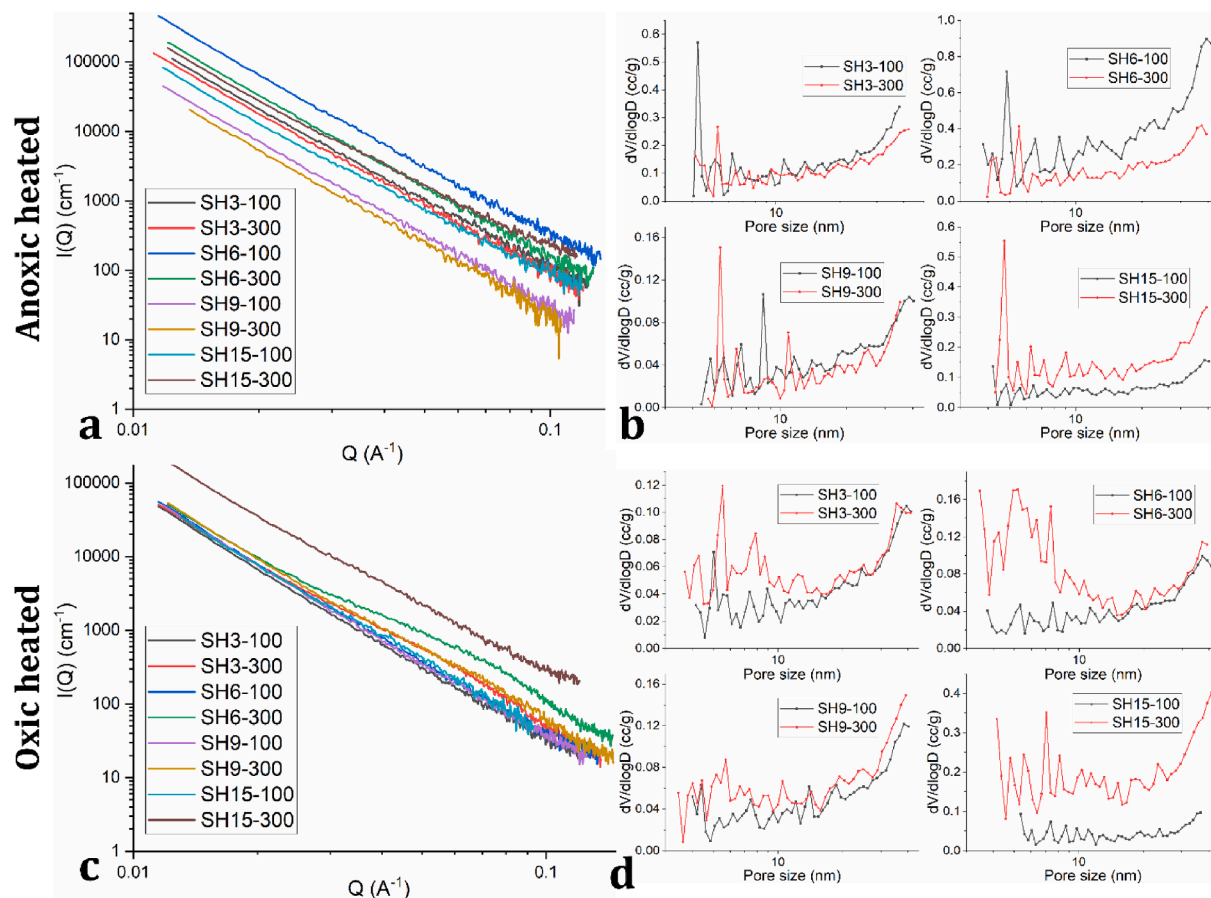
Fig. 6. (a) and (c) scattering of the anoxic and oxic-heated shales, respectively follow a linear trend in a log–log plot. (b) and (d) represent the PSD of anoxic- and oxic-heated shales, respectively, calculated from the SAXS profiles.

3.4. Thermogravimetry

At 350 °C, mass loss starts in the shales and continues until approximately 450 °C (Fig. 8b). Post the primary pyrolysis, SH15 show the highest mass loss (28 %) (Fig. 8a), compared to other shales, which shows 8–13 % mass loss. The exothermic differential mass loss curves show maximum changes between 350 and 550 °C, whereas SH15 and SH3 show bimodal distributions with SH15 showing the highest rate of mass loss (Fig. 8b).

3.5. Pore attributes

3.5.1. Adsorption behavior of thermally combusted shales

The hysteresis patterns shown in Fig. 9a conform with Type-IV isotherm, indicating the dominance of fine mesopores (2–50 nm) [5]. The adsorbed N_2 quantity in the low relative pressure (~0.4) is higher for heated shales. N_2 adsorption is higher in all 300 °C combusted samples with a steeply rising slope at relative pressures between 0.01 and 0.1 and further between 0.8 and 0.99. A pronounced tensile strength hysteretic pattern at 300 °C is also observed (Fig. 9a). The presence of slit-shaped pores is confirmed by H3 and H4 type hysteresis loop at 100 °C and 200 °C heated samples, but this shape changes into H2 when heated at 300 °C; the H2 loop indicating the dominance of bottleneck pores [84]. The CO_2 isotherms display a higher adsorbed volume (Fig. 9b) with increasing temperature and follow the Type-I isotherm pattern, indicating the microporous nature.

Fig. 10a illustrates that the N_2 PSD is multimodal. SH3, SH6, SH15 show peaks around 5–10 nm pore width in the 300 °C treated samples. All samples barring SH9, show an increase in pore volume post 300 °C heat treatment and a gradual decline in pore volume with an increasing

pore width. The N_2 BET surface area for the shale samples ranges from 3.6 to 9 m^2/g for 100 °C, whereas the average pore diameter varies from 7 to 10 nm (Table 2).

The average surface area of the four shales after 100 °C oxic heating is 6.68 m^2/g, which further increases to 16.2 m^2/g after 300 °C oxic heating (Table 2). From 100 °C to 300 °C oxic heating, the average pore volume varies from 0.009 cm^3/g to 0.036 cm^3/g. A multimodal distribution is also noted in CO_2 and N_2 combined DFT PSD (Fig. 10b), where the peaks are around 0.4, 0.6, and 0.8 nm pore width range. N_2 DFT-derived PSD also shows a similar spike in pore volume in the smaller mesopore range as seen in BJH PSD. The DR surface area for all samples varies between 7.26 to 15.64 m^2/g for 100 °C. In the samples treated at 300 °C, the surface area varies from 12.4-39 m^2/g. The total CO_2 pore volume ranges from 0.001 cm^3/g to 0.013 cm^3/g. The modal average DFT micropore diameter for each shale varies between 0.78 nm and 1.1 nm.

3.5.2. Adsorption behavior of anoxic-heated shales

Except SH15, adsorbed N_2 decreases (Fig. 11) for shales subjected to anoxic heating. The isotherm patterns indicate the presence of slit-shaped pores. When heated, the adsorbed N_2 volume decreases in all samples. In contrast, the CO_2 adsorbed volume decreases between 100 °C and 200 °C, but rises at 300 °C (Fig. 11b).

The N_2 PSDs of the shale samples are multimodal (Fig. 12a). Predominant pores are observed around 5, 10, 12, 15, 20, and 28 nm pore width. Unlike combusted samples, the pore volume decreases with increasing temperature in the case of inert heated samples. A multimodal distribution is also noted in CO_2 PSD (Fig. 12b). The BET surface area shows consistent decrease with increasing temperature except SH15 (Table 3).
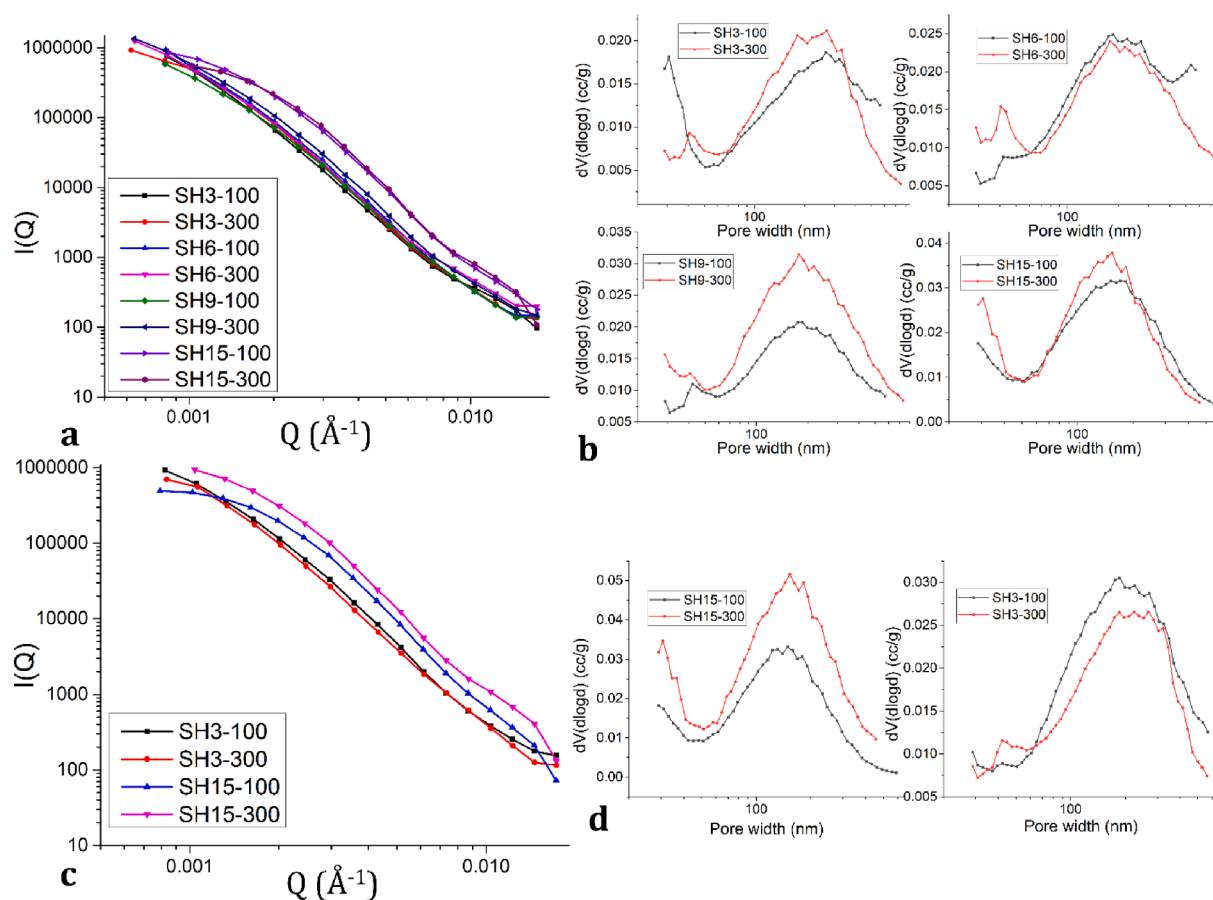
Fig. 7. SANS profiles of the anoxic- (a) and oxic- (c) heated shales. The corresponding PSDs were calculated using PDSP model. (b) Shows the PSDs of the anoxic-heated samples and (d) shows the PSDs of shales heated in presence of oxygen.
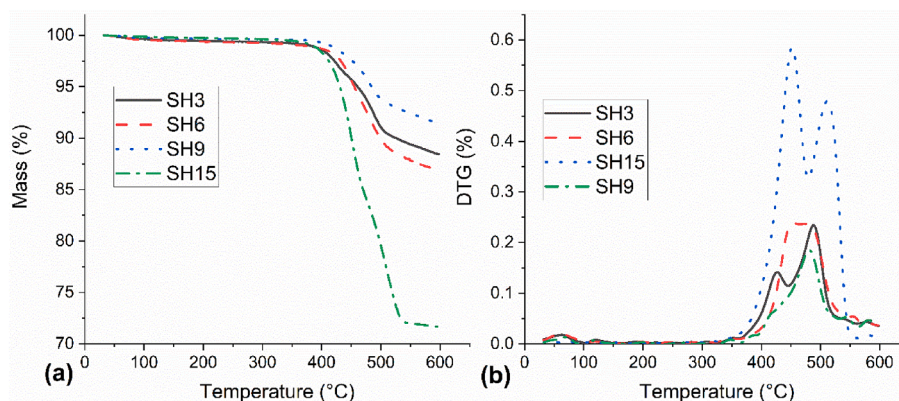
Fig. 8. (a) Cumulative mass-loss of the shales during TG in an inert environment. (b) The differential mass loss behavior (DTG) of the shales.

The DR surface area for all the samples varies between 8.9 to 21.4 m^2/g, for 100 °C. For the samples treated at 300 °C, the surface area varies from 7.5-30 m^2/g.

4. Discussion

The increase in the adsorbed N_2-CO_2 gas volume in the heat-treated samples indicates bigger mesopores in the shale samples. The creation of new micropores in the heated samples is validated by a higher CO_2 adsorbed volume visible in the isotherms (Fig. 10b and 12b). The abrupt change in N_2 adsorbed volume, at 300 °C, establishes the fact about rising adsorbed gas volume with escalating temperature, further asserting an alteration of pore structures, especially pore volume and surface area in the heat-treated samples. The FEG-SEM images (Figs. 4 and 5) captured the phenomenon of growing pore networks through generation of new pores when samples are heated to 300 °C. However, this change is dynamic and occurs differently in the differently heated samples. The presence of bitumen (Fig. 5) in the pyrolyzed samples marks pore blockage, which could be the reason for lower gas adsorption values.

4.1. Thermal breakdown of organic matter

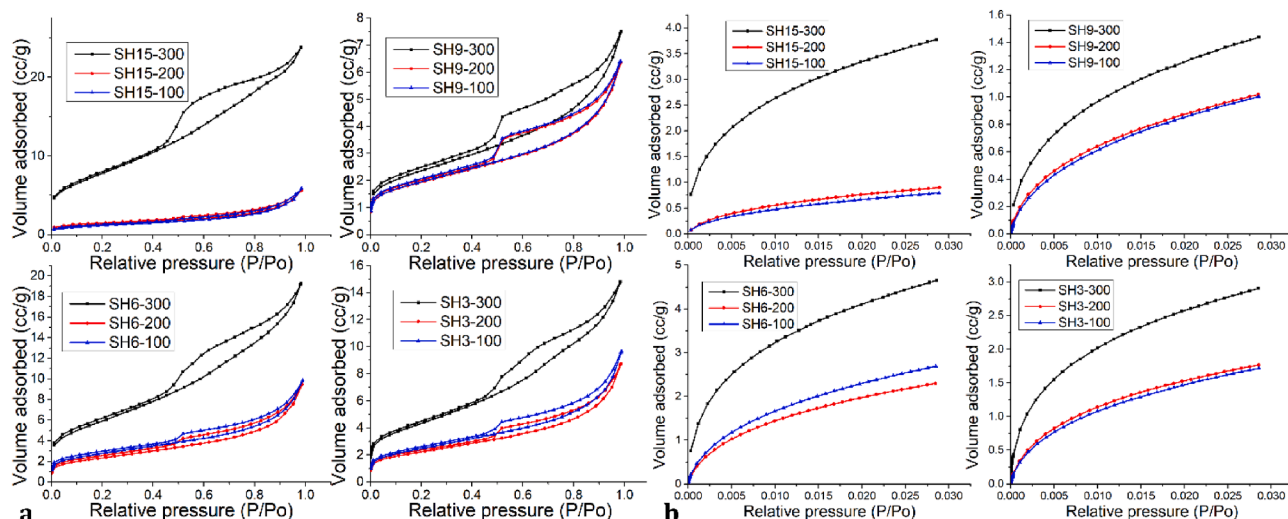Thermal breakdown of the organic matter in shales have been more

Fig. 9. Isotherms of combusted shales (a) N_2 isotherms and desorption hysteresis loops and (b) CO_2 isotherms at 100–300 °C.
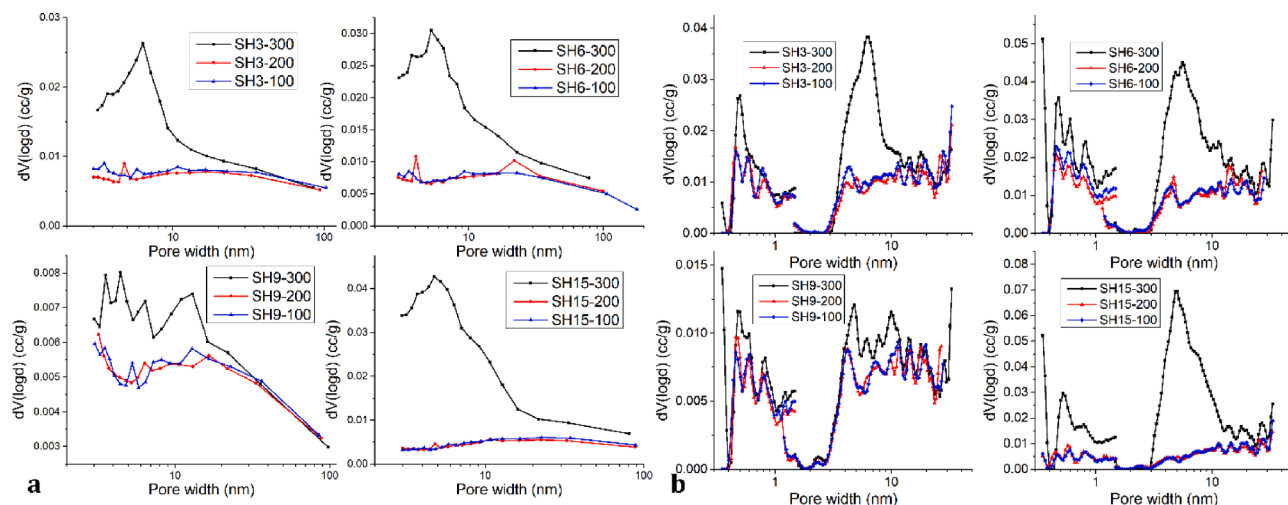

Fig. 10. Combusted samples displaying (a) BJH PSD in all samples at 100 °C-200 °C and 300 °C; (b) shows stitched N_2 and CO_2 DFT PSD for all sample at 100 °C, 200 °C, and 300 °C respectively.

Table 2
Micro- and mesopore characteristics of shales thermally treated in presence of oxygen.

Sample	Temperature (°C)	Mesopore attributes (N_2 adsorption)			Micropore attributes (CO_2 adsorption)	
		Avg pore Width (nm)	BET Surface Area (m²/g)	Mesopore Vol (cc/g)	Micropore Vol (cc/g)	DR Surface Area (m²/g)
SH3	100	7.7	7.80	0.015	0.005	15.6
	200	7.5	7.18	0.014	0.005	16.6
	300	6.6	13.92	0.023	0.008	23.6
SH6	100	6.8	8.95	0.015	0.001	11.3
	200	7.8	7.49	0.015	0.007	22.2
	300	6.3	18.92	0.029	0.013	38.9
SH9	100	6.2	6.39	0.010	0.003	9.3
	200	6.1	6.43	0.009	0.003	9.2
	300	6.0	7.78	0.012	0.004	12.4
SH15	100	10.0	3.59	0.009	0.003	7.2
	200	8.4	4.16	0.009	0.003	8.7
	300	6.0	24.42	0.036	0.010	30

prominent during oxic heating. Chandra et al. (2021) [72] conducted Fourier transform infrared spectroscopy (FTIR) of the studied shales after varying degree of oxic-heating to understand the breakdown of specific organic matter functional groups. FTIR results from the previous study are correlated to the TG study to assess the thermal degradation behavior of kerogen present in shale. The changes in molecular degradation reveal essential information about the dynamics of thermal degradation [85,86]. As evident in the DTG curve (Fig. 8), the clay mineral dehydration occurs initially with maxima around 100 °C. The subsequent reaction is endothermic, as exhibited by the double
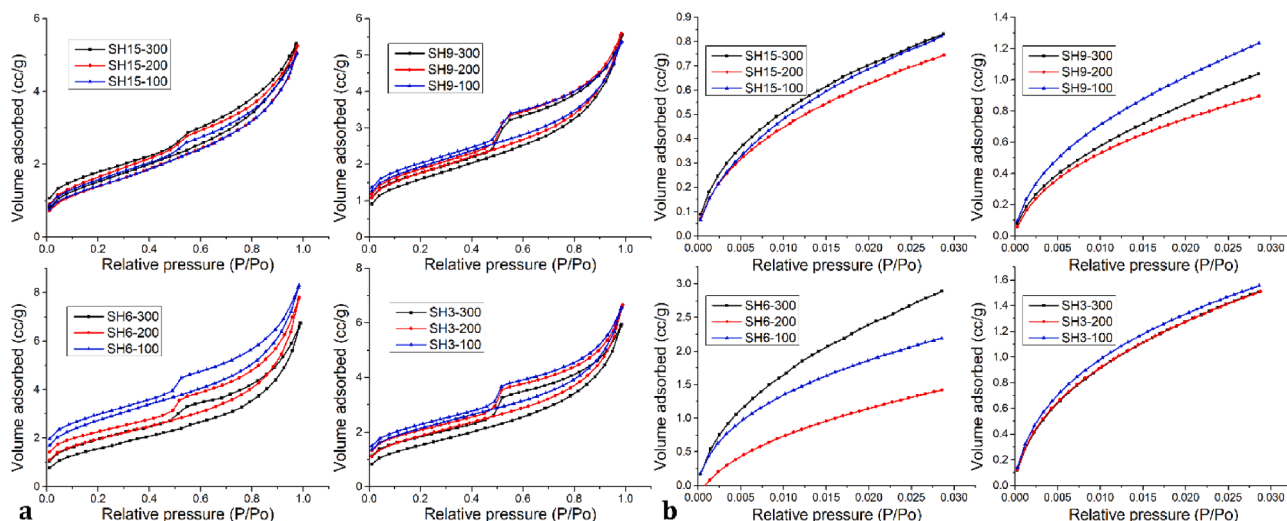
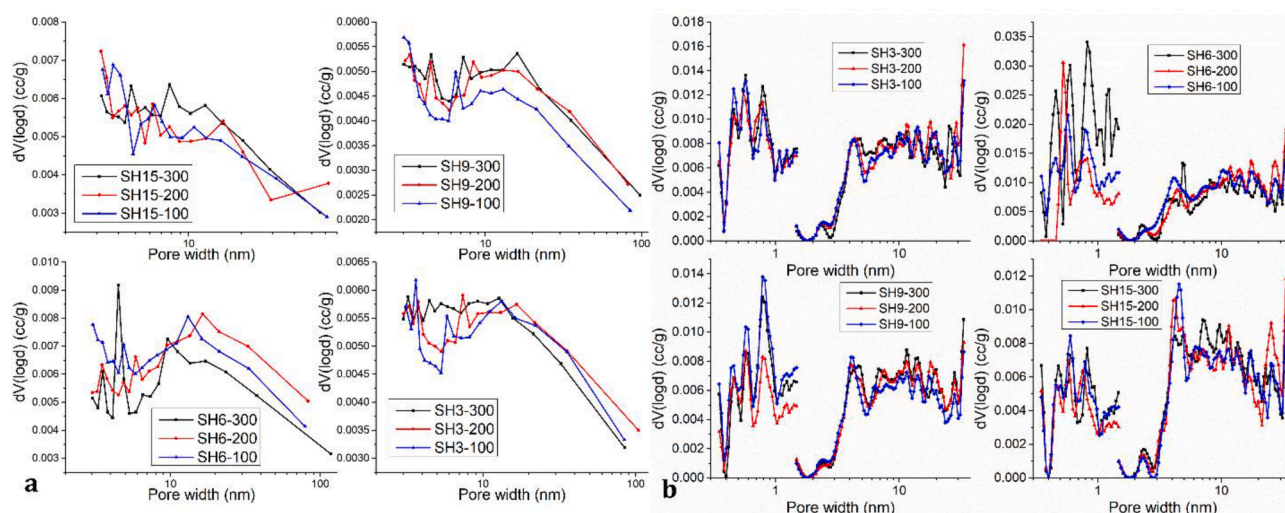**Fig. 11.** Isotherms of thermally treated shales in an inert atmosphere (a) N_2 isotherms (b) CO_2 isotherms.

Fig. 12. 250 µms inert heated samples displaying (a) BJH pore size distributions in all samples (b) stitched N_2 and CO_2 DFT PSD for all the sample at 100 ℃, 200 ℃, and 300 ℃ respectively.

Table 3
Micro- and mesopore characteristics of the shales which are thermally treated in absence of oxygen.

Sample	Temperature (ºC)	Mesopore attributes (N_2 adsorption)			Micropore attributes (CO_2 adsorption)	
		Avg pore Width (nm)	BET Surface Area (m^2/g)	Mesopore Vol (cc/g)	Micropore Vol (cc/g)	DR Surface Area (m^2/g)
SH3	100	5.8	7.07	0.010	0.0033	15
	200	6.9	5.95	0.011	0.0032	14.6
	300	7.8	4.73	0.009	0.0032	14.9
SH6	100	5.7	8.95	0.001	0.0046	21.4
	200	7.6	6.32	0.001	0.0043	20
	300	8.5	4.91	0.001	0.0062	30
SH9	100	5.2	6.46	0.008	0.0026	11.9
	200	6.0	5.78	0.009	0.0019	9.3
	300	6.7	5.12	0.009	0.0023	9.9
SH15	100	6.4	4.90	0.008	0.0017	8.9
	200	6.4	5.13	0.008	0.0017	6.8
	300	6.0	5.53	0.008	0.0015	7.5

peaks in the DTG curve [87], indicating two steps of the pyrolysis process. Total mass loss for pyrolysis reaction in SH15 sample is maximum (30 %) and around 10 % in the other samples. The subsequent reaction is endothermic, related to demineralization of carbonate minerals above 700 °C [87].

The TG/DTG peaks from 400 °C to 600 °C reveal the release of gases due to the breakdown of organic matters in the shale samples during the pyrolysis [88]. The presence of absorption bands at 2400–2240 cm^{-1} at 300 °C suggests the formation of CO_2 due to the thermal cracking of the carbonyl and carboxyl groups present in the kerogen compounds. The

absorption bands exhibit the presence of CO at 2240–2060 cm^{-1}, caused by the breakage of C—O—C and C=O functional groups. The stretching vibration of O—H bonds at 4000–3500 cm^{-1} manifests the release of H$_2$O [86,89]. During pyrolysis, amine or acylamide compounds (N—H functional groups at 3500–3100 cm^{-1}) are produced due to the disintegration of nitrogen functional groups like pyrrole and pyridine. C—H peaks at 1500–400 cm^{-1} in higher temperatures (300 °C), suggesting the decomposition of organic compounds during pyrolysis.

The decomposition of organic matter occurs up to 500 °C along with the generation of H$_2$O and CO$_2$ from kerogen [90]. The HI values of shale samples vary from 54 to 134 (mgHC/g), indicating that the shale is rich in Type-III kerogen [91]. Breaking of hydrogen-rich kerogen causes a considerable mass loss up to 526 °C in the TG curve (Fig. 8) [88,92]. The effect of mass loss is highly pronounced in SH15 which is rich in siderite and other amorphous carbonates. Siderite occurs in source rocks, particularly in the fermentation zones where the preservation of organic matter is enhanced [93]. As SH15 is marked by higher siderite content, the higher reactivity is essentially caused due to the decomposition of siderite during pyrolysis along with the organic matter. Interestingly the thermal decomposition and mass-loss during oxic heating is proportional to the abundance of siderite in each shale. This inference is also corroborated from the thermogravimetric analysis conducted under an inert atmosphere (Fig. 8a). Hence, when pyrolyzed, apart from cracking of carbonyl and carboxyl groups into organic compounds, a high volume of inorganic carbonates and siderites (absorption bands at 2400–2040 cm^{-1}) also decomposes. This causes significant mass loss and generation of strong peaks around 600 °C.

4.2. Changes in pore attributes

Kerogen is a solid organic substance that is insoluble in water and is a complex combination of C, H, S, and O. Thermal decomposition of kerogen eventually transforms kerogen into bitumen and lighter hydrocarbons [94–96]. Yürüm et al. (1985) [97] suggested two stages of kerogen oxidation: the first stage, up to 400 °C, generates char of an aromatic ring system, replaced with some aliphatic and carbonyl groups. Calcium minerals primarily escalate the reactivity of the aromatic portion of any organic matter among the mineral matters. Thus, oxidative reactions alter the kerogen structure by creating more pore spaces, resulting in higher surface area and pore volume (Table 2). The generation of new pores is revealed in CO$_2$ adsorption graphs by the higher adsorption values at 300 °C than that of 100 °C, indicating the formation of smaller pores [98]. Structural changes in clay occur after 300 °C [99–101].

A distinct trend of DTG thermograms was observed during inherent moisture loss and prior to primary pyrolysis (Fig. 8b). A considerable amount of volatiles, accompanied by the disintegration of organic and inorganic matter occurs in the temperature region of 400–600 °C, also known as the primary pyrolysis region [102]. This temperature range attributes to the maximum mass loss because of the release of adsorbed gases like CO$_2$ and CH$_4$ [103], along with the disintegration of labile functional groups which release CO$_2$ and H$_2$O [104]. SH15 (Fig. 8a) shows the highest mass loss (28 %) because of the simultaneous decomposition of organic matter and carbonate minerals. It was also observed that the DTG curve for SH15 is bimodal (peaks at 450 °C and 515 °C), which is due to the discrete degradation of different constituents present in the sample. In general, samples containing carbonate minerals start decomposing nearly at 450 °C up to 600 °C, with a substantial mass loss [105,106], with minimal change in mass after that. The amplitude of the DTG curves has been considered proportional to a sample's reactivity [107], and SH15 amongst the shales showed the highest DTG curve height. A higher concentration of siderite makes this sample more reactive since it decomposes along with the organic matter during pyrolysis, consequently showing more considerable mass loss (TG) and maximum DTG curve height. A shoulder was observed along with the DTG T$_{peak}$ in the sample SH3 (peaks at 425 °C and 490 °C),

which may be due to the heterogeneous organic matter [108]. A unimodal distribution was observed for the sample SH9 with maximum reactions between 350 and 550 °C, while sample SH6 showed a constant mass loss between 425 °C and 500 °C. This study mainly highlights the structural changes of shale composition up to 300 °C, primarily focusing on the changing dynamics of kerogen pores. The change in clay structures occur beyond 300 °C. The thermal decomposition of clay minerals (kaolinite, illite, and montmorillonite), displayed by the Si-O band shifting, happens beyond 600 °C.

Organic matter differs from matrix due to their varying genesis and are treated as a distinct pore type [109–111]. When the SAXS derived PSD (Fig. 6b) is compared with the LPGA-derived mesopore distribution of anoxic-heated shales (Fig. 12b-d), it is evident that the reduction in pore volume is uniform across both accessible and inaccessible pores. However, the difference in the PDSP PSD between 100 °C and 300 °C shales is very minute compared to its LPGA counterpart, which can be explained by the pore blocking with bitumen. When heated over 100 °C, in the absence of oxygen, solid bitumen forms. These resolidified bitumen blocks the newly generated interconnected pore spaces, reducing the surface area and total pore volume. Heating also dries out kerogen, forming shrinkage cracks (Fig. 5d). The shifting of the peak positions (3.5 nm to 4.5 nm in SH3, 4 nm to 4.5 nm in SH6, 8.5 to 10.5 in SH9) towards coarser mesopores in Fig. 6b indicates the expansion of pores under thermal stimulation. Similar peak shifting towards coarser mesopore was observed in a study by Liu and Gadikota, (2018) [31], where they heated shales up to 1150 °C for studying the pore structural evolution. Zhang et al., (2021) [92] has shown minor pore volume increase in shales pyrolyzed up to 400 °C, which corroborates with our observation. The minor change in pore attribute can also be linked with the negligible mass-loss behavior of the shales till 300 °C (Fig. 8a). Contrasting behavior is seen in the combusted shales. The pore volume increase in the finer mesopore range of the SAXS-derived PSD conforms with the LPGA-derived PSD (Fig. 10b-d). The trend of the graphs and the broad peaks signify the merging of multiple smaller mesopores and the formation of new mesopores in the 5–10 nm range. The extent of pore volume increase calculated from both methods indicate a negligible change in pore accessibility due to thermal treatment. On the other hand, the unique perspective of the macropore structural changes shown by the SANS derived PSD (Fig. 7b and d) contradict the behaviour shown in the mesopore ranges in some cases. A crossover was observed in the SANS PSDs around 100 nm pore width range was observed specifically for SH3 and SH6, indicating that the change in pore volume is not uniform across pore sizes. The massive increase in pore volume of SH15 with increase temperature may be attributed the presence of siderite, acting as a catalyst for pore volume increase. For visualizing the scattering behaviour and corresponding PSD trends of the heated shales, we employed two-phase approximation for combining the SANS (low Q) and SAXS (high Q) scattering (Fig. S6a,c). In this consideration, we assume the pore and mineral phase in each of the samples remain consistent for both SANS and SAXS measurements. Employing PSDP method over the whole range provides a clearer outlook towards the *meso* and macropore behaviour (Fig. S6b,d). The slight dip in the pore volume around 40 nm pore width range is an artefact generated due to merging of SAXS and SANS data.

4.3. Changes in surface fractal dimensions

4.3.1. LPGA derived surface fractal dimension

Fractals surfaces have comparable physical features at different scales quantified by fractal dimension (*Ds*), ranging from 2 to 3. When *Ds* is closer to 2, a surface is considered smooth, whereas *Ds* closer to 3 signifies a rough surface [112]. Frenkel-Halsey-Hill (FHH) theory determines the fractal characteristics from the nitrogen adsorption data where *Ds* is dependent upon the adsorption potential (van der Waal's or capillary condensation) [113]. FHH is a reliable method for determining fractal characteristics in mesoporous materials, where the fractal

dimension is determined from the slope of $\ln(\ln(\frac{Po}{P}))$ vs $\ln(V_{ads})$ plot using the following equations:

$$D_2 = 3A + 3 \tag{1a}$$

$$D_1 = A + 3 \tag{1b}$$

where A is the slope of the line trend of $\ln(\ln(\frac{Po}{P}))$ vs $\ln(V_{ads})$ plot. For the coarser mesopore (10–100 nm) region, the capillary condensation is a dominant factor that governs the adsorption process, where Eq (1a) is applicable. However, in the smaller mesopore (2–10 nm) region, as the van der Waal's force governs the adsorption kinetics, Eq (1a) is modified as Eq (1b). For further discussion, we will refer to the fractal dimension of smaller mesopores as D_1 and that of coarser mesopores as D_2.

The mesopore surface fractal dimensions of the combusted shales (Fig S4) shows a slight increase with increasing temperature (Table 4). This reveals that the surface roughness remains unaltered despite the formation of the new pore network in the larger mesopore range. The smaller mesopores also show a higher fractal dimension (D_1) than the coarser mesopores (D_2). However, the newly formed fine mesopores exhibit rougher surfaces, resulting in an upsurge of high values at 300 ℃. Mesopore PSD exhibits very little change in the pore volume in the smaller mesopore range.

The pyrolyzed shale powders show smoother surface (Fig S5) with increasing temperature. Both D_1 and D_2 values are almost identical for the heat-treated shales of varying grain sizes. The newly formed pores resulting from anoxic heating are less rough.

4.3.2. SAXS derived surface fractal dimension

The pore-grain interface in shales is quite complex and exhibit fractal behavior [58,62] depending on the pore connectivity, nature of the pore, and its transport properties. In a fractal system, the density correlation function $\psi(r)$ is represented as [112]:

$$\psi(r) = \frac{1}{V} \int \rho(r + r') \rho(r) dr' \tag{2}$$

where V is the volume of the sample and r is the pore radius.

The scattering intensity decreases as Q^{-m}, where m is a power-law exponent and directly related to the fractal dimension, assuming the pores are fractal in nature [112]. For a fractal pore, the surface fractal follows the expression:

$$D_s = 6 - m \tag{3}$$

where m is the slope of the I(Q) vs Q plot after deducting the upper and lower cut-off to preserve the fractality of the pores [114]. Similar to the FHH fractal dimension, Ds varies between 2 and 3 depending on the pore surface roughness. The fractal dimension of the shales derived from

SAXS data (Table 4) shows a similar trend as that of the LPGA-derived surface fractal, i.e., the pore surface becomes smoother with increasing temperature in the oxic environment and vice versa.

4.4. Effect of CO₂-shale interaction on shale pores

Studies have reported that ScCO₂ interaction with shale pores can cause permanent alteration in shale pore morphology and overall pore volume. The extent of change depends on the organic content, thermal maturity, mineral content, and time of saturation. Yin et al. [115] reported that after 30 days of ScCO₂ saturation, significant dissolution of organic matter and clay minerals is evident due to interaction with ScCO₂ which results in reduced adsorption potential in micro and mesopore range. Interestingly, the changes reported are limited only to pore volume and surface area; no changes in pore morphology was reported in their study which contradicts the finding of Sanguinito et al. [116] where the authors reported change in pore morphology due to etching on pore surface through cyclic dissolution and precipitation of carbonates. They attributed this change to the effect of dissolution and CO₂ induced swelling behavior. Similar observation was reported in other studies where the change in pore volume due to swelling and dissolution also causes reduction in mechanical properties of shale and the extent of change is proportional to the time of ScCO₂ saturation [117–119]. A detailed investigation of elemental mobility in shales post-ScCO₂ and water treatment [120] reveals that the primary dissolution happens in the carbonates, mobilizing Ca and Mg elements, whereas the secondary preference is given to clay minerals, mobilizing Na, K and Al elements. Contrary to previous studies, they reported a minor change in pore morphology, inferred through the change in hysteresis behavior of N₂ LPGA isotherms. A comparative study of gaseous CO₂ and ScCO₂ saturation reported that the effect of adsorption and swelling governs the change in pore attributes during gaseous CO₂ treatment, whereas ScCO₂ saturation facilitates the dissolution of minerals [116,121]. It is also noteworthy to mention that the effect of ScCO₂ saturation alone on shale pores is completely different from the combined effect of ScCO₂ and brine. Presence of CO₂ in brine changes the pH of solution, resulting in HCO₃– formation, facilitating deposition of kaolinite, gypsum, amorphous globules [122] and dissolution of feldspars. The combined effect of such chemical alterations results in almost 4 % increase in porosity, whereas dry ScCO₂ treatment can cause up to 20 % reduction in total pore volume and 36 % reduction in surface area [123]. The effect of ScCO₂ also changes depending on the type of kerogen and studies have shown that the change in micropore structure in shales for Type I kerogen is mostly due to adsorption-induced swelling. However, for Type II kerogen (TOC < 3 %), the change is governed by pore framework reorganization due to dissolution of minerals [124]. A molecular dynamics (MD) based study of mineral-ScCO₂ and OM-ScCO₂ interaction has shown that the solid–liquid friction is lowest for OM-ScCO₂, resulting in a larger slip length, which allows ScCO₂ to penetrate even smaller micropores in shales very easily [125]. A pressure-dependent

Table 4
Surface fractal dimension of shale mesopores at varying temperatures under different heating environments. D_1 and D_2 represent surface fractals of finer mesopores (2–10 nm) and coarser mesopores (10–100 nm), respectively. SAXS derived fractal dimensions are represented as D_S.

| Sample ID | N₂-LPGA derived | | | | SAXS derived | |
| | Combustion | | Pyrolysis | | Combustion | Pyrolysis |
	D_1	D_2	D_1	D_2	D_{SX}	D_{SX}
SH3-100	2.5	2.25	2.61	2.31	2.73	2.76
SH3-200	2.49	2.22	2.55	2.28		
SH3-300	2.5	2.34	2.48	2.22	2.83	2.71
SH6-100	2.51	2.31	2.59	2.31	2.78	2.75
SH6-200	2.47	2.19	2.53	2.13		
SH6-300	2.52	2.37	2.44	2.22	2.9	2.7
SH9-100	2.55	2.28	2.62	2.4	2.72	2.58
SH9-200	2.54	2.31	2.58	2.31		
SH9-300	2.59	2.34	2.53	2.31	2.85	2.56
SH15-100	2.49	1.98	2.47	2.22	2.43	2.6
SH15-200	2.53	2.1	2.43	2.22		
SH15-300	2.5	2.46	2.47	2.19	2.8	2.6

Table 5
Change in micro and mesopore attributes of shales between 100 °C and 300 °C oxic and anoxic heating. All values are represented in percentage.

Sample	BET surface area	Mesopore volume	Micropore volume	DR surface area
Oxic heating				
SH3	+78.46	+53.33	+60.00	+51.28
SH6	+111.40	+93.33	+1200.00	+244.25
SH9	+21.75	+20.00	+33.33	+33.33
SH15	+580.22	+300.00	+233.33	+316.67
Anoxic heating				
SH3	−33.10	−10.00	−3.03	−0.67
SH6	−45.14	0.00	34.78	40.19
SH9	−20.74	−12.50	−11.54	−16.81
SH15	12.86	0.00	−11.76	−15.73
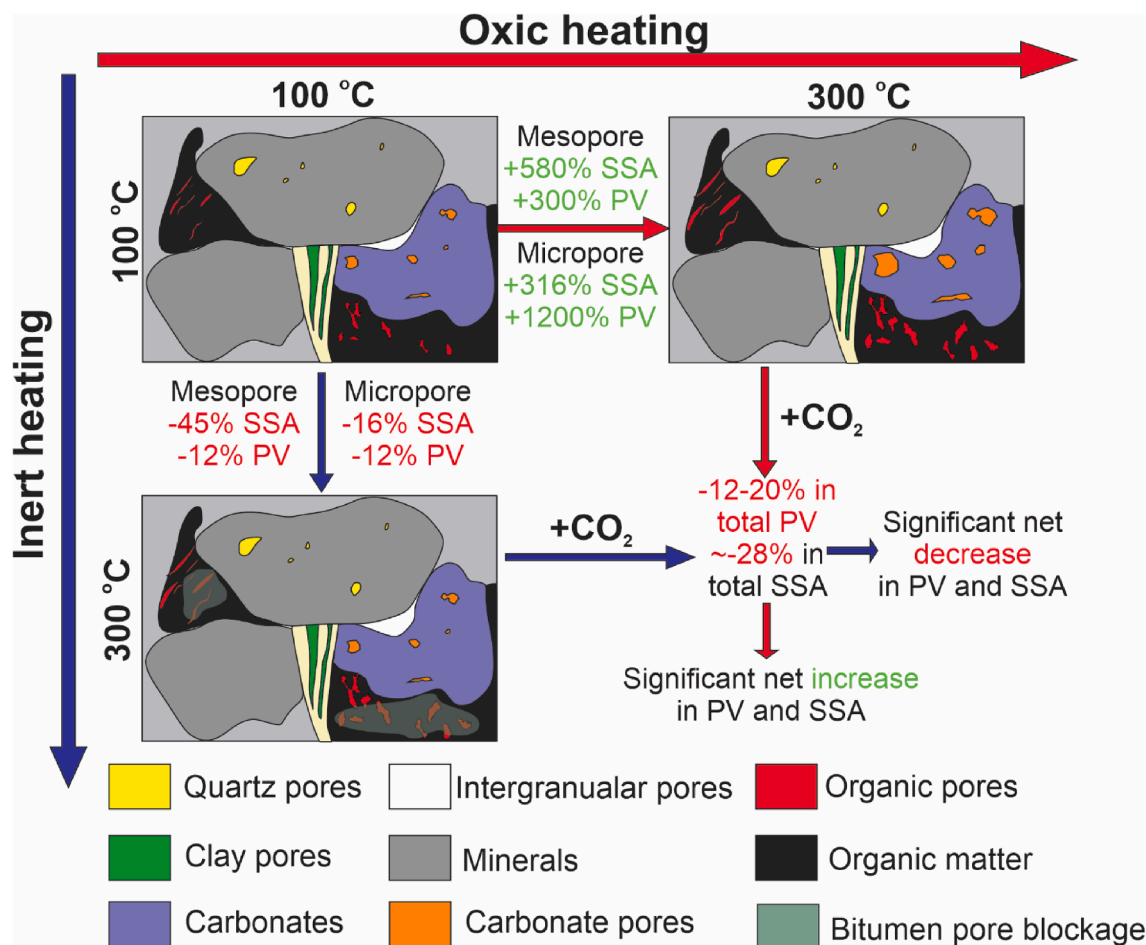
Fig. 13. A schematic representation of the change in pore attributes of anoxic and oxic heated shales after interaction with CO_2. Features in this figure are not to scale.

sensitivity study by [126] explains that with higher pressure of $ScCO_2$ saturation, the fluid density increases, accelerating the pore scale changes, resulting in a drastic increase in seepage channels.

Our study shows that the increase in surface area and pore volume in shales post oxic heat treatment up to 300 °C is consistent across micro and mesopores (Table 5).

While micropores show>300 % increase in surface area after oxic heating, mesopores show up to 580 % increase in surface area and 300 % increase in pore volume. In the micropore region, a massive increase of up to 1200 % in pore volume can also be observed. The extent of increase is directly proportional to the presence of siderite. On the other hand, up to 45 % reduction in mesopore surface area and up to 12 % reduction in mesopore volume is observed for anoxic heated shales (except SH15). In the micropore domain also, the reduction in pore attributes is consistent except SH6. The significant increase in pore volume and surface area post oxic heating will not only counter the reduction in pore attributes due to $ScCO_2/CO_2$ interaction with shale, but will also increase the pore connectivity and net storage capacity in shales. On the contrary, anoxic heating of shales, which reduces the pore volume and surface area will be a poor choice for enhancing the CO_2 storage capacity in shales, as the pore volume will further reduce due to interaction with $ScCO_2/CO_2$ (Fig. 13).

5. Conclusions

This study provides insight on the dynamics of pore evolution under thermal stimulation both in presence and absence of oxygen. The changes in pore attributes under anoxic heating provide insights on the dynamics of pore alteration during thermal maturation of shale under reservoir condition. The changes in pore attributes under oxic heating elucidate the changes in organic matter hosted pores during thermal stimulation-based enhanced shale gas recovery and CO_2 storage applications. The conclusions from this study are summarized as follows:

1. SEM images reveal that the organic pores show substantial enhancement in connectivity when heated up to 300 ºC in presence of oxygen. Mobilization of bitumen and its deposition in smaller mesopores during anoxic heating result in 20–50 % reduction in accessible mesopore and micropore surface area, 30–35 % increase in average mesopore width and subsequent decrease in accessible pore volume.

2. The SANS derived PSDs indicate that smaller mesopores are prone to lose accessibility due to bitumen deposition. The thermogravimetry data exhibit considerable mass loss around 450 °C, which is attributed to the breaking of hydrogen-rich Type-III kerogen. The higher reactivity of SH15 is catalyzed by the decomposition of siderite along with the organic matter as evident from S3′ pyrogram. High thermal response of siderite emphasizes the alteration in organic matter and can offset the reduction in pore volume during anoxic heating.

3. Oxic-heated shales show a higher N_2 and CO_2 adsorption potential, indicating coalition and generation of micro and mesopores, which is also evident from the peak shift of PDSP size distribution. This phenomenon along with honeycomb-shaped pore formation leads to the changes in the pore volume and surface area with successive heating.

4. The surface roughness of the shale pores remains mostly unchanged, although new mesopores are formed that have rougher interfaces. The smaller mesopores exhibit a higher fractal dimension (D_1) than coarser mesopores (D_2). The inert-heated shale samples show a lowering in surface roughness with increasing temperature. However, SAXS-derived surface fractal increases with oxic heating and minutely decreases with anoxic heating. Newly formed pores due to anoxic heating have lesser roughness, due to amalgamation of existing pores and surface smoothening.

5. Oxic-heated shales causing enhancement in pore volume and surface area is a suitable method for increasing pore connectivity and thereby increasing the feasibility of CO_2 storage. Such methods can be applied in depleted shale reservoirs as high-temperature treatment may alter the organic matter present in shales.

CRediT authorship contribution statement

Debanjan Chandra: Data curation, Formal analysis, Investigation, Methodology, Writing – original draft. **Tuli Bakshi:** Validation, Investigation, Writing – original draft. **Jitendra Bahadur:** Investigation, Methodology, Resources, Validation, Writing – review & editing. **Bodhisatwa Hazra:** Investigation, Formal analysis. **Vikram Vishal:** Conceptualization, Methodology, Validation, Project administration, Supervision, Writing – review & editing. **Shubham Kumar:** Investigation. **Debasis Sen:** Writing – review & editing. **T.N. Singh:** Writing – review & editing.

Declaration of Competing Interest

The authors declare that they have no known competing financial interests or personal relationships that could have appeared to influence the work reported in this paper.

Data availability

Data will be made available on request.

Appendix A. Supplementary data

Supplementary data to this article can be found online at https://doi.org/10.1016/j.fuel.2022.125877.

References

[1] Bernard S, Brown L, Wirth R, Schreiber A, Schulz H-M, Horsfield B, et al. FIB-SEM and TEM Investigations of an Organic-rich Shale Maturation Series from the Lower Toarcian Posidonia Shale, Germany<subtitle>Nanoscale Pore System and Fluid-rock Interactions</subtitle>. Electron Microsc Shale Hydrocarb Reserv 2013. https://doi.org/10.1306/13391705m1023583.

[2] Clarkson CR, Solano N, Bustin RM, Bustin AMM, Chalmers GRL, He L, et al. Pore structure characterization of North American shale gas reservoirs using USANS/SANS, gas adsorption, and mercury intrusion. Fuel 2013;103:606–16. https://doi.org/10.1016/j.fuel.2012.06.119.

[3] Mastalerz M, Hampton LB, Drobniak A, Loope H. Significance of analytical particle size in low-pressure N2 and CO2 adsorption of coal and shale. Int J Coal Geol 2017;178:122–31. https://doi.org/10.1016/j.coal.2017.05.003.

[4] Labani MM, Rezaee R, Saeedi A, Al HA. Evaluation of pore size spectrum of gas shale reservoirs using low pressure nitrogen adsorption, gas expansion and mercury porosimetry: A case study from the Perth and Canning Basins, Western Australia. J Pet Sci Eng 2013;112:7–16. https://doi.org/10.1016/j.petrol.2013.11.022.

[5] Kuila U, Prasad M. Specific surface area and pore-size distribution in clays and shales. Geophys Prospect 2013;61:341–62. https://doi.org/10.1111/1365-2478.12028.

[6] Bai J, Kang Y, Chen M, Liang L, You L, Li X. Investigation of multi-gas transport behavior in shales via a pressure pulse method. Chem Eng J 2019. https://doi.org/10.1016/j.cej.2018.10.197.

[7] Chen W, Lei Y, Chen Y, Sun J. Pyrolysis and Combustion Enhance Recovery of Gas for Two China Shale Rocks. Energy & Fuels 2016;30:10298–305. https://doi.org/10.1021/acs.energyfuels.6b02274.

[8] Deng H, Hu X, Li HA, Luo B, Wang W. Improved pore-structure characterization in shale formations with FESEM technique. J Nat Gas Sci Eng 2016. https://doi.org/10.1016/j.jngse.2016.08.063.

[9] Ji W, Song Y, Jiang Z, Meng M, Liu Q, Chen L, et al. Fractal characteristics of nano-pores in the Lower Silurian Longmaxi shales from the Upper Yangtze Platform, south China. Mar Pet Geol 2016;78:88–98. https://doi.org/10.1016/j.marpetgeo.2016.08.023.

[10] Jamaluddin AKM, Bennion DB, Thomas FB, Ma TY. Application of heat treatment to enhance permeability in tight gas reservoirs. J Can Pet Technol 2000. https://doi.org/10.2118/00-11-01.

[11] Karacan O, Kok MV. Pyrolysis Analysis of Crude Oils and Their Fractions. Energy Fuels 1997;11:385–91. https://doi.org/10.1021/EF960162+.

[12] Versan Kök M, Özbas E, Karacan O, Hicyilmaz C. Effect of particle size on coal pyrolysis. J Anal Appl Pyrolysis 1998;45:103–10. https://doi.org/10.1016/s0165-2370(98)00063-1.

[13] Hazra B, Karacan CÖ, Tiwari DM, Singh PK, Singh AK. Insights from Rock-Eval analysis on the influence of sample weight on hydrocarbon generation from Lower Permian organic matter rich rocks, West Bokaro basin. India Mar Pet Geol 2019;106:160–70. https://doi.org/10.1016/j.marpetgeo.2019.05.006.

[14] Kök MV, Karacan O. Pyrolysis analysis and kinetics of crude oils. J Therm Anal Calorim 1998;52:781–8. https://doi.org/10.1023/A:1010114624345.

[15] Chapiro G, Bruining J. Combustion enhance recovery of shale gas. J Pet Sci Eng 2015;127:179–89. https://doi.org/10.1016/j.petrol.2015.01.036.

[16] Chen W, Lei Y, Ma L, Yang L. Experimental Study of High Temperature Combustion for Enhanced Shale Gas Recovery. Energy Fuels 2017;31:10003–10. https://doi.org/10.1021/acs.energyfuels.7b00762.

[17] Chen W, Lei Y, Chen Y, Sun J. Pyrolysis and Combustion Enhance Recovery of Gas for Two China Shale Rocks. Energy Fuels 2016. https://doi.org/10.1021/acs.energyfuels.6b02274.

[18] Chen W, Zhou Y, Yang L, Zhao N, Lei Y. Experimental study of low-temperature combustion characteristics of shale rocks. Combust Flame 2018;194:285–95. https://doi.org/10.1016/j.combustflame.2018.04.033.

[19] Chen W, Lei Y, Ma L, Yang L. Experimental Study of High Temperature Combustion for Enhanced Shale Gas Recovery. Energy Fuels 2017. https://doi.org/10.1021/acs.energyfuels.7b00762.

[20] Rigby SP, Jahan H, Stevens L, Uguna C, Snape C, Macnaughton B, et al. Pore structural evolution of shale following thermochemical treatment. Mar Pet Geol 2020. https://doi.org/10.1016/j.marpetgeo.2019.104058.

[21] Kang Z, Zhao Y, Yang D. Review of oil shale in-situ conversion technology. Appl Energy 2020;269:115121. https://doi.org/10.1016/j.apenergy.2020.115121.

[22] Cai Y, Liu D, Pan Z, Yao Y, Li J, Qiu Y. Pore structure and its impact on CH4 adsorption capacity and flow capability of bituminous and subbituminous coals from Northeast China. Fuel 2013;103:258–68. https://doi.org/10.1016/j.fuel.2012.06.055.

[23] Mastalerz M, Schimmelmann A, Drobniak A, Chen Y. Porosity of Devonian and Mississippian New Albany Shale across a maturation gradient: Insights from organic petrology, gas adsorption, and mercury intrusion. Am Assoc Pet Geol Bull 2013;97:1621–43. https://doi.org/10.1306/04011312194.

[24] Munson EO. Reservoir characterization of the Duvernay Formation, Alberta : a pore- to basin-scale investigation. University of British Columbia; 2015.

[25] Begum M, Yassin MR, Dehghanpour H. Effect of kerogen maturity on organic shale wettability: A Duvernay case study. Mar Pet Geol 2019;110:483–96. https://doi.org/10.1016/J.MARPETGEO.2019.07.012.

[26] Yassin MR, Begum M, Dehghanpour H. Organic shale wettability and its relationship to other petrophysical properties: A Duvernay case study. Int J Coal Geol 2017;169:74–91. https://doi.org/10.1016/j.coal.2016.11.015.

[27] Lan Q, Dehghanpour H, Wood J, Sanei H. Wettability of the Montney Tight Gas Formation. SPE Reserv Eval Eng 2015;18:417–31. https://doi.org/10.2118/171620-PA.

[28] Zhang L, Sun M, Lv Q, Ukaomah CF, Hu Q, Yu B, et al. Evolution of Shale Microstructure under in Situ Heat Treatment: Synchrotron Small-Angle X-ray Scattering. Energy Fuels 2021;35:4345–57. https://doi.org/10.1021/ACS.ENERGYFUELS.1C00091/ASSET/IMAGES/LARGE/EF1C00091_0010.JPEG.

[29] Zhu J, Yi L, Yang Z, Duan M. Three-dimensional numerical simulation on the thermal response of oil shale subjected to microwave heating. Chem Eng J 2021;407:127197. https://doi.org/10.1016/J.CEJ.2020.127197.

[30] Vishal V, Rizwan M, Mahanta B, Pradhan SP, Singh TN. Temperature effect on the mechanical behavior of shale: Implication for shale gas production. Geosystems and Geoenvironment 2022;1:100078. https://doi.org/10.1016/J.GEOGEO.2022.100078.

[31] Liu M, Gadikota G. Probing the Influence of Thermally Induced Structural Changes on the Microstructural Evolution in Shale using Multiscale X-ray Scattering Measurements. Energy Fuels 2018;32:8193–201. https://doi.org/10.1021/ACS.ENERGYFUELS.8B01486/ASSET/IMAGES/LARGE/EF-2018-01486G_0009.JPEG.

[32] Tiwari P, Deo M, Lin CL, Miller JD. Characterization of oil shale pore structure before and after pyrolysis by using X-ray micro CT. Fuel 2013;107:547–54. https://doi.org/10.1016/j.fuel.2013.01.006.

[33] Guo Y, Huang L, Li X, Chen J, Sun J. Experimental investigation on the effects of thermal treatment on the physical and mechanical properties of shale. J Nat Gas Sci Eng 2020;82:103496. https://doi.org/10.1016/J.JNGSE.2020.103496.

[34] Bai F, Sun Y, Liu Y, Guo M. Evaluation of the porous structure of Huadian oil shale during pyrolysis using multiple approaches. Fuel 2017;187:1–8. https://doi.org/10.1016/J.FUEL.2016.09.012.

[35] Jiang C, Yang W, Duan M, Wang G, Xu Z. Pore structure alteration and permeability enhancement of shale under cyclic thermal impacts. Powder Technol 2022;396:385–93. https://doi.org/10.1016/J.POWTEC.2021.11.010.

[36] Zhu GP, Yao J, Sun H, Zhang M, Xie MJ, Sun ZX, et al. The numerical simulation of thermal recovery based on hydraulic fracture heating technology in shale gas reservoir. J Nat Gas Sci Eng 2016;28:305–16. https://doi.org/10.1016/J.JNGSE.2015.11.051.

[37] Godec M, Koperna G, Petrusak R, Oudinot A. Enhanced Gas Recovery and CO2 Storage in Gas Shales: A Summary Review of its Status and Potential. Energy Procedia 2014;63:5849–57. https://doi.org/10.1016/J.EGYPRO.2014.11.618.

[38] Jia B, Chen Z, Xian C. Investigations of CO2 storage capacity and flow behavior in shale formation. J Pet Sci Eng 2022;208:109659. https://doi.org/10.1016/J.PETROL.2021.109659.

[39] Rani S, Padmanabhan E, Prusty BK. Review of gas adsorption in shales for enhanced methane recovery and CO2 storage. J Pet Sci Eng 2019;175:634–43. https://doi.org/10.1016/J.PETROL.2018.12.081.

[40] Bielicki JM, Langenfeld JK, Tao Z, Middleton RS, Menefee AH, Clarens AF. The geospatial and economic viability of CO2 storage in hydrocarbon depleted fractured shale formations. Int J Greenh Gas Control 2018;75:8–23. https://doi.org/10.1016/J.IJGGC.2018.05.015.

[41] Myshakin EM, Singh H, Sanguinito S, Bromhal G, Goodman AL. Numerical estimations of storage efficiency for the prospective CO2 storage resource of shales. Int J Greenh Gas Control 2018;76:24–31. https://doi.org/10.1016/J.IJGGC.2018.06.010.

[42] Godec M, Koperna G, Petrusak R, Oudinot A. Potential for enhanced gas recovery and CO2 storage in the Marcellus Shale in the Eastern United States. Int J Coal Geol 2013;118:95–104. https://doi.org/10.1016/J.COAL.2013.05.007.

[43] Xu R, Zeng K, Zhang C, Jiang P. Assessing the feasibility and CO2 storage capacity of CO2 enhanced shale gas recovery using Triple-Porosity reservoir model. Appl Therm Eng 2017;115:1306–14. https://doi.org/10.1016/J.APPLTHERMALENG.2017.01.062.

[44] Goodman A, Sanguinito S, Kutchko B, Natesakhawat S, Cvetic P, Allen AJ. Shale pore alteration: Potential implications for hydrocarbon extraction and CO2 storage. Fuel 2020;265:116930. https://doi.org/10.1016/J.FUEL.2019.116930.

[45] Pan Y, Hui D, Luo P, Zhang Y, Sun L, Wang K. Experimental Investigation of the Geochemical Interactions between Supercritical CO2 and Shale: Implications for CO2 Storage in Gas-Bearing Shale Formations. Energy Fuels 2018;32:1963–78. https://doi.org/10.1021/ACS.ENERGYFUELS.7B03074/ASSET/IMAGES/LARGE/EF-2017-03074W_0015.JPEG.

[46] Fatah A, Bennour Z, Ben Mahmud H, Gholami R, Hossain MM. A Review on the Influence of CO2/Shale Interaction on Shale Properties: Implications of CCS in Shales. Energies 2020, Vol 13, Page 3200 2020;13:3200. https://doi.org/10.3390/EN13123200.

[47] Liu F, Ellett K, Xiao Y, Rupp JA. Assessing the feasibility of CO2 storage in the New Albany Shale (Devonian–Mississippian) with potential enhanced gas recovery using reservoir simulation. Int J Greenh Gas Control 2013;17:111–26. https://doi.org/10.1016/J.IJGGC.2013.04.018.

[48] Louk K, Ripepi N, Luxbacher K, Gilliland E, Tang X, Keles C, et al. Monitoring CO2 storage and enhanced gas recovery in unconventional shale reservoirs: Results from the Morgan County, Tennessee injection test. J Nat Gas Sci Eng 2017;45:11–25. https://doi.org/10.1016/J.JNGSE.2017.03.025.

[49] Liu J, Liang X, Xue Y, Yao K, Fu Y. Numerical evaluation on multiphase flow and heat transfer during thermal stimulation enhanced shale gas recovery. Appl Therm Eng 2020;178:115554. https://doi.org/10.1016/J.APPLTHERMALENG.2020.115554.

[50] Bauman JH, Deo M. Simulation of a conceptualized combined pyrolysis, in situ combustion, and CO 2 storage strategy for fuel production from green river oil shale. Energy Fuels 2012;26:1731–9. https://doi.org/10.1021/EF2017072/ASSET/IMAGES/EF-2011-017072_M010.GIF.

[51] Varma AK, Mishra DK, Samad SK, Prasad AK, Panigrahi DC, Mendhe VA, et al. Geochemical and organo-petrographic characterization for hydrocarbon generation from Barakar Formation in Auranga Basin. India Int J Coal Geol 2018;186:97–114. https://doi.org/10.1016/j.coal.2017.12.002.

[52] Mendhe VA, Mishra S, Varma AK, Kamble AD, Bannerjee M, Sutay T. Gas reservoir characteristics of the Lower Gondwana Shales in Raniganj Basin of Eastern India. J Pet Sci Eng 2017;149:649–64. https://doi.org/10.1016/j.petrol.2016.11.008.

[53] Gee ER. The geology and coal resources of the Raniganj coalfield. Gov India: Cent Publ Branch; 1932.

[54] Paul DK. Petrology and geochemistry of the Salma dike, Raniganj coalfield (Lower Gondwana), eastern India: linkage with Rajmahal or Deccan volcanic activity? J Asian Earth Sci 2005;25:903–13. https://doi.org/10.1016/J.JSEAES.2004.09.007.

[55] Fox SCS. The Gondwana System and related formations. Branch: Gov. Indian Cent. Publ; 1931.

[56] Bhattacharya B, Bandyopadhyay S, Mahapatra S, Banerjee S. Record of tide-wave influence on the coal-bearing Permian Barakar Formation, Raniganj Basin. India

[57] Sediment Geol 2012;267–268:25–35. https://doi.org/10.1016/j.sedgeo.2012.05.006.

[57] Chandra D, Vishal V, Bahadur J, Sen D. A novel approach to identify accessible and inaccessible pores in gas shales using combined low-pressure sorption and SAXS/SANS analysis. Int J Coal Geol 2020;228:103556. https://doi.org/10.1016/J.COAL.2020.103556.

[58] Radlinski AP, Mastalerz M, Hinde AL, Hainbuchner M, Rauch H, Baron M, et al. Application of SAXS and SANS in evaluation of porosity, pore size distribution and surface area of coal. Int J Coal Geol 2004;59:245–71. https://doi.org/10.1016/j.coal.2004.03.002.

[59] Mazumder S, Sen D, Saravanan T, Vijayaraghavan PR. Performance and calibration of the newly installed medium resolution double crystal based small-angle neutron scattering instrument at trombay. J Neutron Res 2001;9:39–57. https://doi.org/10.1080/10238160108200241.

[60] Mazumder S, Aswal VK, Sen D, Bahadur J, Kumar S, Das A. Mesoscopic structural investigations using neutrons at Trombay. Neutron News 2014;25:26–30. https://doi.org/10.1080/10448632.2014.870800.

[61] Rezaeyan A, Pipich V, Busch A. MATSAS : a small-angle scattering computing tool for porous systems. J Appl Crystallogr 2021;54:697–706. https://doi.org/10.1107/s1600576721000674.

[62] Vishal V, Chandra D, Bahadur J, Sen D, Hazra B, Mahanta B, et al. Interpreting Pore Dimensions in Gas Shales Using a Combination of SEM Imaging, Small-Angle Neutron Scattering, and Low-Pressure Gas Adsorption. Energy and Fuels 2019;33:4835–48. https://doi.org/10.1021/ACS.ENERGYFUELS.9B00442/ASSET/IMAGES/LARGE/EF-2019-00442P_0011.JPEG.

[63] Holmes R, Rupp EC, Vishal V, Wilcox J. Selection of Shale Preparation Protocol and Outgas Procedures for Applications in Low-Pressure Analysis. Energy Fuels 2017;31:9043–51. https://doi.org/10.1021/acs.energyfuels.7b01297.

[64] Hazra B, Wood DA, Vishal V, Varma AK, Sakha D, Singh AK. Porosity controls and fractal disposition of organic-rich Permian shales using low-pressure adsorption techniques. Fuel 2018;220:837–48. https://doi.org/10.1016/j.fuel.2018.02.023.

[65] Hazra B, Wood DA, Vishal V, Singh AK. Pore Characteristics of Distinct Thermally Mature Shales: Influence of Particle Size on Low-Pressure CO2 and N2 Adsorption. Energy Fuels 2018;32:8175–86. https://doi.org/10.1021/acs.energyfuels.8b01439.

[66] Hazra B, Chandra D, Singh AK, Varma AK, Mani D, Singh PK, et al. Comparative pore structural attributes and fractal dimensions of Lower Permian organic-matter-bearing sediments of two Indian basins: Inferences from nitrogen gas adsorption. Energy Sources, Part A: Recovery, Utilization, and Environmental Effects 2019;41(24):2975–88.

[67] Chandra D, Vishal V. A Comparative Analysis of Pore Attributes of Sub-Bituminous Gondwana Coal from the Damodar and Wardha Valleys: Implication for Enhanced Coalbed Methane Recovery. Energy Fuels 2022.

[68] Thommes M, Kaneko K, Neimark AV, Olivier JP, Rodriguez-Reinoso F, Rouquerol J, et al. Physisorption of gases, with special reference to the evaluation of surface area and pore size distribution (IUPAC Technical Report). Pure Appl Chem 2015;87:1051–69. https://doi.org/10.1515/pac-2014-1117.

[69] Ravikovitch PI, Vishnyakov A, Russo R, Neimark AV. Unified Approach to Pore Size Characterization of Microporous Carbonaceous Materials from N2, Ar, and CO2Adsorption Isotherms†. Langmuir 2000;16:2311–20. https://doi.org/10.1021/la991011c.

[70] Chandra D, Vishal V. A comparison of nano-scale pore attributes of Barakar Formation gas shales from Raniganj and Wardha Basin, India using low pressure sorption and FEG-SEM analysis. J Nat Gas Sci Eng 2020;81:103453. https://doi.org/10.1016/J.JNGSE.2020.103453.

[71] Chandra D, Vishal V, Debbarma A, Banerjee DS, Pradhan SP, Mishra MK. Role of composition and depth on pore attributes of Barakar Formation gas shales of Ib Valley, India using a combination of low pressure sorption and image analysis. Energy & Fuels 2020:acs.energyfuels.0c00746-acs.energyfuels.0c00746. https://doi.org/10.1021/acs.energyfuels.0c00746.

[72] Chandra D, Bakshi T, Vishal V. Thermal effect on pore characteristics of shale under inert and oxic environments: Insights on pore evolution. Microporous Mesoporous Mater 2021;316:110969. https://doi.org/10.1016/J.MICROMESO.2021.110969.

[73] Rock-Eval 6 Operator Manual 2003.

[74] Carvajal-Ortiz H, Gentzis T. Critical considerations when assessing hydrocarbon plays using Rock-Eval pyrolysis and organic petrology data: Data quality revisited. Int J Coal Geol 2015;152:113–22. https://doi.org/10.1016/j.coal.2015.06.001.

[75] Hazra B, Singh DP, Chakraborty P, Singh PK, Sahu SG, Adak AK. Using rock-eval S4Tpeak as thermal maturity proxy for shales. Mar Pet Geol 2021;127:104977. https://doi.org/10.1016/j.marpetgeo.2021.104977.

[76] Hazra B, Singh DP, Crosdale PJ, Singh V, Singh PK, Gangopadhyay M, et al. Critical insights from Rock-Eval analysis of vitrains. Int J Coal Geol 2021;238:103717. https://doi.org/10.1016/j.coal.2021.103717.

[77] Jarvie D, Claxto B. ABSTRACT: Oil and Shale Gas from the Barnett Shale, Ft. Worth Basin, Texas. Am Assoc Pet Geol Bull 2001;85. https://doi.org/10.1306/8626e28d-173b-11d7-8645000102c1865d.

[78] Wust RAJ, Hackley PC, Nassichuk BR, Willment N, Brezovski R. Vitrinite Reflectance Versus Pyrolysis Tmax Data: Assessing Thermal Maturity in Shale Plays with Special Reference to the Duvernay Shale Play of the Western Canadian Sedimentary Basin, Alberta, Canada. Soc Pet Eng - Asia Pacific Unconv Resour Conf Exhib 2013 Deliv Abund Energy a Sustain Futur 2013;1:347–57. https://doi.org/10.2118/167031-MS.

[79] Behar F, Beaumont V, Penteado HDB. Rock-Eval 6 technology: performances and developments. Oil Gas Sci Technol 2001;56(2):111–34.

[80] Hazra B, Singh DP, Chakraborty P, Das H, Singh V, Sahu SG, et al. Structural and thermal properties of vitrain lithotype in coal-inferences from TG-DTG-DSC, Rock-Eval and X-ray diffraction. J Earth Syst Sci 2022;131(2):1–12.

[81] Shi Y, Yassin MR, Yuan L, Dehghanpour H. Modelling imbibition data for determining size distribution of organic and inorganic pores in unconventional rocks. Int J Coal Geol 2019;201:26–43. https://doi.org/10.1016/J.COAL.2018.11.010.

[82] Milliken KL, Rudnicki M, Awwiller DN, Zhang T. Organic matter-hosted pore system, Marcellus Formation (Devonian). Pennsylvania Am Assoc Pet Geol Bull 2013;97:177–200. https://doi.org/10.1306/07231212048.

[83] Loucks RG, Reed RM, Ruppel SC, Jarvie DM. Morphology, Genesis, and Distribution of Nanometer-Scale Pores in Siliceous Mudstones of the Mississippian Barnett Shale. J Sediment Res 2009;79:848–61. https://doi.org/10.2110/jsr.2009.092.

[84] Guo X. Major factors controlling the shale gas accumulations in Wufeng-Longmaxi Formation of the Pingqiao Shale Gas Field in Fuling Area, Sichuan Basin. China J Nat Gas Geosci 2019;4:129–38. https://doi.org/10.1016/j.jnggs.2019.06.002.

[85] Xu T, Huang X. Study on combustion mechanism of asphalt binder by using TG–FTIR technique. Fuel 2010;89:2185–90. https://doi.org/10.1016/j.fuel.2010.01.012.

[86] Fan C, Yan J, Huang Y, Han X, Jiang X. XRD and TG-FTIR study of the effect of mineral matrix on the pyrolysis and combustion of organic matter in shale char. Fuel 2015;139:502–10. https://doi.org/10.1016/j.fuel.2014.09.021.

[87] Labus M, Matyasik I. Application of different thermal analysis techniques for the evaluation of petroleum source rocks. J Therm Anal Calorim 2019;136:1185–94. https://doi.org/10.1007/s10973-018-7752-3.

[88] Labus M, Lempart M. Studies of Polish Paleozoic shale rocks using FTIR and TG/DSC methods. J Pet Sci Eng 2018;161:311–8. https://doi.org/10.1016/j.petrol.2017.11.057.

[89] Yan J, Jiang X, Han X, Liu J. A TG–FTIR investigation to the catalytic effect of mineral matrix in oil shale on the pyrolysis and combustion of kerogen. Fuel 2013;104:307–17. https://doi.org/10.1016/j.fuel.2012.10.024.

[90] Han H, Zhong N, Huang C, Zhang W. Pyrolysis kinetics of oil shale from northeast China: Implications from thermogravimetric and Rock-Eval experiments. Fuel 2015;159:776–83. https://doi.org/10.1016/j.fuel.2015.07.052.

[91] Peters KE, Cassa MR. Applied Source Rock Geochemistry: Chapter 5: Part II. Essential Elements 1994;77:93–120.

[92] Zhang J, Ding Y, Du W, Lu K, Sun L. Study on pyrolysis kinetics and reaction mechanism of Beizao oil shale. Fuel 2021;296:120696. https://doi.org/10.1016/j.fuel.2021.120696.

[93] Lafargue E, Marquis F, Pillot D. Rock-Eval 6 Applications in Hydrocarbon Exploration, Production, and Soil Contamination Studies. Rev l'Institut Français Du Pétrole 1998;53:421–37. https://doi.org/10.2516/ogst:1998036.

[94] Schrodt JT, Ocampo A. Variations in the pore structure of oil shales during retorting and combustion. Fuel 1984. https://doi.org/10.1016/0016-2361(84)90219-9.

[95] Han H, Cao Y, Chen S, Lu J, Huang C, Zhu H, et al. Influence of particle size on gas-adsorption experiments of shales: An example from a Longmaxi Shale sample from the Sichuan Basin. China Fuel 2016;186:750–7. https://doi.org/10.1016/j.fuel.2016.09.018.

[96] Bai F, Sun Y, Liu Y, Guo M. Evaluation of the porous structure of Huadian oil shale during pyrolysis using multiple approaches. Fuel 2017. https://doi.org/10.1016/j.fuel.2016.09.012.

[97] Yürüm Y, Kramer R, Levy M. Interaction of kerogen and mineral matrix of an oil shale in an oxidative atmosphere. Thermochim Acta 1985;94:285–93. https://doi.org/10.1016/0040-6031(85)85272-2.

[98] Tang X, Zhang J, Jin Z, Xiong J, Lin L, Yu Y, et al. Experimental investigation of thermal maturation on shale reservoir properties from hydrous pyrolysis of Chang 7 shale. Ordos Basin Mar Pet Geol 2015;64:165–72. https://doi.org/10.1016/j.marpetgeo.2015.02.046.

[99] Grim RE, Bradley WF. INVESTIGATION OF THE EFFECT OF HEAT ON THE CLAY MINERALS ILLITE AND MONTMORILLONITE*. J Am Ceram Soc 1940;23:242–8. https://doi.org/10.1111/j.1151-2916.1940.tb14263.x.

[100] Sun Q, Zhang W, Qian H. Effects of high temperature thermal treatment on the physical properties of clay. Environ Earth Sci 2016;75:610. https://doi.org/10.1007/s12665-016-5402-2.

[101] Stevenson CM, Gurnick M. Structural collapse in kaolinite, montmorillonite and illite clay and its role in the ceramic rehydroxylation dating of low-fired earthenware. J Archaeol Sci 2016;69:54–63. https://doi.org/10.1016/j.jas.2016.03.004.

[102] Raghuvanshi G, Chakraborty P, Hazra B, Adak AK, Singh PK, Singh AK, et al. Pyrolysis and combustion behavior of few high-ash Indian coals. Int J Coal Prep Util 2020:1–21. https://doi.org/10.1080/19392699.2020.1855582.

[103] Liu J, Ma J, Luo L, Zhang H, Jiang X. Pyrolysis of superfine pulverized coal. Part 5. Thermogravimetric analysis. Energy Convers Manag 2017;154:491–502. https://doi.org/10.1016/j.enconman.2017.11.041.

[104] Song H, Liu G, Wu J. Pyrolysis characteristics and kinetics of low rank coals by distributed activation energy model. Energy Convers Manag 2016;126:1037–46. https://doi.org/10.1016/j.enconman.2016.08.082.

[105] Zhang H, Bai J, Kong L, Li X, Bai Z, Li W. Behavior of Minerals in Typical Shanxi Coking Coal during Pyrolysis. Energy Fuels 2015;29:6912–9. https://doi.org/10.1021/acs.energyfuels.5b01191.

[106] Zhang X, Han Y, Li Y, Sun Y. Effect of Heating Rate on Pyrolysis Behavior and Kinetic Characteristics of Siderite. Minerals 2017;7:211. https://doi.org/10.3390/min7110211.

[107] Ghetti P, Ricca L, Angelini L. Thermal analysis of biomass and corresponding pyrolysis products. Fuel 1996;75:565–73. https://doi.org/10.1016/0016-2361(95)00296-0.

[108] Mohalik NK, Lester E, Lowndes IS. Review of experimental methods to determine spontaneous combustion susceptibility of coal – Indian context. Int J Mining, Reclam Environ 2016;31:301–32. https://doi.org/10.1080/17480930.2016.1232334.

[109] Nie H, Jin Z, Zhang J. Characteristics of three organic matter pore types in the Wufeng-Longmaxi Shale of the Sichuan Basin. Southwest China Sci Rep 2018;8:7014. https://doi.org/10.1038/s41598-018-25104-5.

[110] Curtis ME, Sondergeld CH, Ambrose RJ, Rai CS. Microstructural investigation of gas shales in two and three dimensions using nanometer-scale resolution imaging. Am Assoc Pet Geol Bull 2012;96:665–77. https://doi.org/10.1306/08151110188.

[111] Bernard S, Horsfield B, Schulz H-M, Wirth R, Schreiber A, Sherwood N. Geochemical evolution of organic-rich shales with increasing maturity: A STXM and TEM study of the Posidonia Shale (Lower Toarcian, northern Germany). Mar Pet Geol 2012;31:70–89. https://doi.org/10.1016/j.marpetgeo.2011.05.010.

[112] Mandelbrot BB. The fractal geometry of nature. San Francisco, CA: 1982.

[113] Prusty BK, Turlapati VY, Bakshi T. Detailed pore structure study of Damodar valley and upper Assam basin shales using fractal analysis. Energy Fuels 2020;34:14001–11. https://doi.org/10.1021/acs.energyfuels.0c02785.

[114] Bale HD, Schmidt PW. Small-Angle X-Ray-Scattering Investigation of Submicroscopic Porosity with Fractal Properties. Phys Rev Lett 1984;53:596–9. https://doi.org/10.1103/PhysRevLett.53.596.

[115] Yin H, Zhou J, Jiang Y, Xian X, Liu Q. Physical and structural changes in shale associated with supercritical CO2 exposure. Fuel 2016;184:289–303. https://doi.org/10.1016/J.FUEL.2016.07.028.

[116] Sanguinito S, Goodman A, Tkach M, Kutchko B, Culp J, Natesakhawat S, et al. Quantifying dry supercritical CO2-induced changes of the Utica Shale. Fuel 2018;226:54–64. https://doi.org/10.1016/J.FUEL.2018.03.156.

[117] Ao X, Lu Y, Tang J, Chen Y, Li H. Investigation on the physics structure and chemical properties of the shale treated by supercritical CO2. J CO2 Util 2017;20:274–81. https://doi.org/10.1016/J.JCOU.2017.05.028.

[118] Cheng Y, Zeng M, Lu Z, Du X, Yin H, Yang L. Effects of Supercritical CO2 Treatment Temperatures on Mineral Composition, Pore Structure and Functional Groups of Shale: Implications for CO2 Sequestration. Sustain 2020, Vol 12, Page 3927 2020;12:3927. https://doi.org/10.3390/SU12093927.

[119] Qin C, Jiang Y, Zhou J, Zuo S, Chen S, Liu Z, et al. Influence of supercritical CO2 exposure on water wettability of shale: Implications for CO2 sequestration and shale gas recovery. Energy 2022;242:122551. https://doi.org/10.1016/J.ENERGY.2021.122551.

[120] Luo X, Ren X, Wang S. Supercritical CO2-water-shale interactions and their effects on element mobilization and shale pore structure during stimulation. Int J Coal Geol 2019;202:109–27. https://doi.org/10.1016/J.COAL.2018.12.007.

[121] Lu Y, Zhou J, Li H, Chen X, Tang J. Different Effect Mechanisms of Supercritical CO2on the Shale Microscopic Structure. ACS Omega 2020;5:22568–77. https://doi.org/10.1021/ACSOMEGA.0C03200/ASSET/IMAGES/ACSOMEGA.0C03200.SOCIAL.JPEG_V03.

[122] Rezaee R, Saeedi A, Iglauer S, Evans B. Shale alteration after exposure to supercritical CO2. Int J Greenh Gas Control 2017;62:91–9. https://doi.org/10.1016/J.IJGGC.2017.04.004.

[123] Huang X, Zhao YP, Wang X, Pan L. Adsorption-induced pore blocking and its mechanisms in nanoporous shale due to interactions with supercritical CO2. J Pet Sci Eng 2019;178:74–81. https://doi.org/10.1016/J.PETROL.2019.03.018.

[124] Dai X, Wang M, Wei C, Zhang J, Wang X, Zou M. Factors affecting shale microscopic pore structure variation during interaction with supercritical CO2. J CO2 Util 2020;38:194–211. https://doi.org/10.1016/J.JCOU.2020.01.021.

[125] Wang S, Javadpour F, Feng Q. Fast mass transport of oil and supercritical carbon dioxide through organic nanopores in shale. Fuel 2016;181:741–58. https://doi.org/10.1016/J.FUEL.2016.05.057.

[126] Jiang Y, Luo Y, Lu Y, Qin C, Liu H. Effects of supercritical CO2 treatment time, pressure, and temperature on microstructure of shale. Energy 2016;97:173–81. https://doi.org/10.1016/J.ENERGY.2015.12.124.